A novel inertial-aided visible light positioning system using modulated LEDs and unmodulated lights as landmarks

Qing Liang[1], *Member, IEEE*, Yuxiang Sun[2], *Member, IEEE*, Lujia Wang[1], *Member, IEEE*, and Ming Liu[1], *Senior Member, IEEE*

***Abstract*—Indoor localization with high accuracy and efficiency has attracted much attention. Due to visible light communication (VLC), the LED lights in buildings, once modulated, hold great potential to be ubiquitous indoor localization infrastructure. However, this entails retrofitting the lighting system and is hence costly in wide adoption. To alleviate this problem, we propose to exploit modulated LEDs and existing unmodulated lights as landmarks. On this basis, we present a novel inertial-aided visible light positioning (VLP) system for lightweight indoor localization on resource-constrained platforms, such as service robots and mobile devices. With blob detection, tracking, and VLC decoding on rolling-shutter camera images, a visual frontend extracts two types of blob features, i.e., mapped landmarks (MLs) and opportunistic features (OFs). These are tightly fused with inertial measurements in a stochastic cloning sliding-window extended Kalman filter (EKF) for localization. We evaluate the system by extensive experiments. The results show that it can provide lightweight, accurate, and robust global pose estimates in real-time. Compared with our previous ML-only inertial-aided VLP solution, the proposed system has superior performance in terms of positional accuracy and robustness under challenging light configurations like sparse ML/OF distribution.**

***Note to Practitioners*—This paper is motivated by the problem that many existing visible light positioning (VLP) systems require high cost environmental modifications, i.e., replacing a large portion of original lights with modulated LEDs as beacons. To reduce costs in wide adoption, we seek to use fewer modulated LEDs if possible. Accordingly, we present a novel inertial-aided VLP system that uses both modulated LEDs and unmodulated lights as landmarks. Like in other VLP systems, the successfully decoded LEDs provide absolute pose measurements for global localization. Unmodulated lights and the LEDs with decoding failures provide relative motion constraints, allowing the reduction of pose drift during the outage of modulated LEDs. Owing to the tightly coupled sensor fusion by filtering, the system can provide efficient and accurate localization when modulated LEDs are sparse. The system is lightweight to run on resource-constrained platforms. For practical deployment of our system at scale, creating LED maps accurately and efficiently remains a problem. It is desired to develop automated LED mapping solutions in future work.**

*This work was supported by the National Natural Science Foundation of China, under grant No. U1713211, Zhongshan Municipal Science and Technology Bureau Fund, under project ZSST21EG06, Collaborative Research Fund by Research Grants Council Hong Kong, under Project No. C4063-18G, and Department of Science and Technology of Guangdong Province Fund, under Project No. GDST20EG54, awarded to Prof. Ming Liu (*Corresponding author: Ming Liu*).

[1]Qing Liang, Lujia Wang and Ming Liu are with the Department of Electronic and Computer Engineering, The Hong Kong University of Science and Technology, Hong Kong (email: {qliangah,eewanglj,eelium}@ust.hk).

[2]Yuxiang Sun is with the Department of Mechanical Engineering, The Hong Kong Polytechnic University, Hung Hom, Hong Kong (e-mail: yx.sun@polyu.edu.hk, sun.yuxiang@outlook.com).

***Index Terms*—Indoor localization, sensor fusion, visible light positioning, visible light communication, extended Kalman filter, aided inertial navigation, service robots.**

I. Introduction

LOCALIZATION is fundamental to many robot tasks (e.g., path-planning, navigation, and manipulation) and a wide variety of location-based services like augmented reality and pedestrian navigation in large venues. Platforms like service robots and mobile devices can have low-end sensors on board and limited processing capabilities in computation, memory, and power. To aid long-term operation, both the localization accuracy and efficiency count. Among established sensors, the camera and micro-electro-mechanical inertial measurement unit (MEMS IMU) provide rich information for metric state estimation while being small, low-cost, and power-efficient [1]. There are many developed visual-inertial odometry (VIO) algorithms [2]–[7] capable of real-time accurate six-degrees-of-freedom (DoF) pose estimation. Some are lightweight to run on mobile devices, as revealed by ARKit [8] and ARCore [9]. However, VIO suffers from unbounded drift over time [1]. Global pose corrections are needed for long-term operation.

When people or robots localize in frequently-visited scenes (e.g., shopping malls), prior knowledge from prebuilt maps or localization infrastructure like Global Positioning System (GPS) can assist. Visual (-inertial) localization against visual feature maps has attracted wide research interest [10]–[14], and state-of-the-arts achieve high accuracy and efficiency. Still, the performance could suffer from dynamic changes in the environment [15]–[17] in the short-term (e.g., moving objects) or long-term (e.g., appearance or lighting). Visual (-inertial) localization in 3D light detection and ranging (LiDAR) maps is another promising solution [18], [19]. Yet, dealing with LiDAR maps requires high onboard computation and memory, hindering their use on resource-constrained platforms. Combined with local odometry, the absolute GPS measurements are often effective for outdoor localization [20]–[25]. These methods can show good accuracy and efficiency. Note the GPS-like infrastructure provides known data associations [26], quick and reliable, by using domain-specific knowledge from radio communications or visual coding patterns [27]. This eases the state estimation problem, enables instant relocalization, and promotes processing efficiency.

With the growing adoption of LED lights in buildings for energy-efficient lighting, LEDs hold great potential to become

a kind of *indoor GPS* owing to visible light communication (VLC) technologies [28]–[30]. Normally, LEDs are densely and uniformly spaced on ceilings for illumination. As solid-state devices, LEDs can be instantly modulated to transmit data by visible light. The high-frequency light changes are invisible to human eyes but are perceivable by photodiodes or cameras. Modulated LEDs broadcast their unique identities by VLC, allowing quick and reliable data association. They play the dual role of lighting and localization beacons. The LED locations are fixed and less vulnerable to environmental changes. The LED map hence remains effective for long-term localization after one-time registration. Modulated LEDs of known locations enable high-accuracy 3D localization due to the line-of-sight light propagation [31]–[33]. This is broadly known as visible light positioning (VLP) in the literature.

Many low-cost cameras with rolling shutters can seamlessly act as VLC receivers [33]–[35]. It is trivial to compute the camera pose by perspective-n-point (PnP) if more than three LED features are detected in one camera frame. Such vision-only methods [32], [33] can suffer in reality due to insufficient LED observations. The number of decodable LEDs in a frame is limited by a few factors such as the geometry layout and density of lights, the ceiling height, the camera's field of view (FoV), and the maximum VLC decoding distance. To tackle this issue, some recent works [36]–[38] have adopted IMU measurements as a complement. In our previous work [38], we presented an integrated VLC-inertial localization system using an extended Kalman filter (EKF). In situations in which there is a lack of LEDs, this system can provide satisfying results by tightly fusing LED features and inertial measurements.

As in [38], we aim to perform localization with a minimal visual-inertial sensor suite, commonly used for monocular VIO [7]. We focus on using ceiling lights as landmarks to develop a lightweight localization system for indoor applications. Be noticed that the benefits of having known data associations by VLC require the cost of artificial modifications, e.g., upgrading existing lights with modulated LEDs. To reduce costs for large-scale applications, we seek to rely on as few modulated LEDs as possible. In our case, the camera is mainly used as a VLC receiver, which requires a very short exposure time for operation [35]. As such, naturally occurring visual features are hardly detectable. Meanwhile, the regular unmodulated lights existing in buildings, despite being less rich or informative than natural features, can be readily detected. The derived blob features add certain visual cues for relative pose estimation, and in this way constrain pose drift in the absence of modulated LEDs. In light of this, we propose to make full use of the blob features detectable from lights, both modulated and unmodulated, by our underexposed camera.

In this paper, with modulated LEDs and unmodulated lights as landmarks in buildings, we propose a novel inertial-aided VLP system using a rolling-shutter camera for lightweight global localization on resource-constrained platforms. From observations of lights, we extract two types of blob features: mapped landmarks (MLs) and opportunistic features (OFs). The former has associated global 3D positions while the latter does not. Specifically, MLs correspond to modulated LEDs registered in a prior map[1] and successfully decoded during runtime. We can explicitly resolve the long-term data associations by VLC and know from the map the associated global positions. MLs provide absolute geometric constraints to correct any accumulated pose errors in the long run. They are essential to our proposed system as well as to many other VLP systems [31]–[33]. OFs, on the other hand, come mainly from the unmodulated lights and in part from those modulated LEDs with decoding failures. We can resolve only the short-term data associations by temporal feature tracking. This way, OFs provide relative motion constraints to help reduce pose drift during ML outages, thereby benefiting the overall localization. OFs are sometimes optional to our system depending on the ML outage situations. The blob features are tightly integrated with inertial measurements by a stochastic cloning sliding window EKF [2] for pose estimation. To the best of our knowledge, the approach we propose is the first inertial-aided VLP system that fully exploits modulated LEDs and unmodulated lights as landmarks within a sliding window filter-based framework. This gives us the flexibility to replace a proportion of the original lights (e.g., at strategic locations like entrances) and not all as in conventional VLP systems, while achieving comparable localization performance with much-reduced cost. We restrict the contributions of this work to the context of VLP and highlight them as follows:

- A novel inertial-aided VLP system for lightweight indoor localization that fully exploits modulated LEDs and unmodulated lights as landmarks. The sensor measurements (MLs, OFs, and inertial) are tightly fused within a stochastic cloning sliding-window EKF framework. It is capable of performance comparable to conventional VLP systems at minimal infrastructure cost.
- A blob tracking-assisted decoding strategy for rolling-shutter VLC mechanisms in VLP use case. Blob tracking improves the decoding success during camera motion with the introduced short-term data association.
- Design choices of using delayed ML measurements from blob tracking and using unmodulated lights as OFs to provide motion constraints for VLP.
- Extensive system evaluation by real-world experiments in various scenarios showing the effectiveness and performance gains of our system. It has achieved superior positional accuracy and robustness under challenging light conditions (e.g., very sparse ML/OF distribution) when compared to an ML-only VLP solution [38].

The remainder of this paper is organized as follows. Section II introduces the related work. Section III shows the overview of the proposed system. Section IV and Section V describes key components of the system, including an image processing frontend and an EKF-based pose estimator. Section VI and Section VII presents experimental results and discussions of limitations, respectively. Section VIII concludes this paper. The acronyms throughout this paper can be found in Table. I.

[1]Solving a localization problem, we assume that all modulated LEDs for MLs have been preregistered on an LED feature map before operation.

TABLE I: List of acronyms.

AGC	automatic gain control	OF	opportunistic feature
ATE	absolute trajectory error	OOK	on-off keying
DoF	degrees of freedom	PID	permanent identity
EKF	extended Kalman filter	PnP	perspective-n-point
FoV	field of view	RANSAC	random sample consensus
GPS	Global Positioning System	RMSE	root mean squared error
IMU	inertial measurement unit	ROI	region of interest
LiDAR	light detection and ranging	SCKF	stochastic cloning Kalman filter
MEMS	micro-electro-mechanical systems	TID	temporal identity
ML	mapped landmark	VIO	visual-inertial odometry
MOSFET	metal-oxide-semiconductor field-effect transistor	VLC	visible light communication
MSCKF	multi-state constraint Kalman filter	VLP	visible light positioning

II. Related Work

There is a rich body of literature on indoor localization. For fundamentals and comprehensive surveys, readers can refer to [28]–[30], [39]–[46]. In this section, we only review those closely related to our proposed system, e.g., indoor localization using lights as landmarks in Section II-A and visual-inertial localization with global measurements in Section II-B.

A. Indoor Localization using Lights as Landmarks

Much research effort has been put into indoor localization using lights, including both modulated LEDs and unmodulated light sources, as environmental features.

1) Modulated LEDs: VLP takes advantage of known data associations conveyed by VLC. Often, VLP systems employ modulated LEDs as location beacons, use cameras [32], [33], [47]–[49] or photodiodes [31], [50], [51] as light sensors, recognize each beacon using its unique identity from VLC decoding, measure bearings or ranges to visible beacons, and determine the sensor location from geometry measurements. Photodiode-based VLP systems require accurate propagation channel modeling and can be less accurate or robust than their camera-based counterparts. For camera-based systems, vision-only methods like PnP need three or more LED features to fix a 6-DoF pose. Their use is limited in the case of insufficient LEDs. In such cases, fusion of inertial measurements assists, in loosely- [31], [36] or tightly- [37], [38] coupled ways. These systems heavily rely on modulated LEDs for operation and hence incur extensive modifications of lighting infrastructure. To alleviate this issue, researchers have attempted to reuse existing light sources without modification.

2) Unmodulated lights: Compared to modulated LEDs, the lack of communications adds to the challenge of obtaining data associations for unmodulated lights. These lights can relate to certain feature descriptions for data association. LiTell [52] is a camera-based localization system that uses unmodulated fluorescent lights. It exploits the characteristic frequency (CF), which is diverse among lights due to manufacturing tolerances, from the light spectrum as a unique identifier. CF features are extracted from high-resolution images of raw format and matched to a built feature map for light identification. Using a customized photodiode receiver, the follow-up Pulsar [53] can work from LEDs whose CF features are much weaker. However, due to temperature fluctuation, grid voltage variation, and aging, such features tend to be less reliable over time [52]. iLAMP [54] exploits the spatial radiance patterns extracted from light images of raw format as feature descriptors, owing to the diversity from manufacturing variations. As reported by [52], [54], the feature extraction and matching therein are computationally demanding, partly due to processing raw images. This can cause high latencies in location updates (e.g., a few hundred ms) and differs from our goal of developing a lightweight system for resource-constrained platforms.

Methods also exist which do not identify individual lights explicitly. In [55], [56], lights are characterized by physical locations without any feature description. The overhead lights can be detected using photodiode sensors on smartphones and by finding peaks in received light signals while people are walking by. To handle inherent identity ambiguities, the authors resorted to using a particle filter for solving 2D sensor poses and the latent data association. Due to the lack of explicit data associations, [55], [56] cannot provide instant relocalization as other VLP systems do.

3) Both types: Our goal is to keep the benefits of modulated LEDs for lightweight localization on resource-constrained devices while minimizing the retrofit cost for environment modification. This motivates us to make full use of both modulated and unmodulated lights. In literature, the closest work to ours in concept is [57]. The authors use an upward-facing fisheye camera for 2D localization by observing ceiling lights of known locations. Two modulated LEDs are added for instant pose initialization. To obtain correspondences for other lights, a set of light blobs are detected and matched to the ceiling light map. Here, we focus on 6-DoF localization with a common pinhole camera. Orthogonal to others, we treat unmodulated lights as opportunistic features without knowing their absolute locations. They instead provide relative motion constraints to help reduce pose drift when modulated LEDs are unavailable. We note the camera adopted by [57] can sample specific pixels at high speed (with a period of $20.8\,\mu\mathrm{s}$) while being costly. VLC is realized by analyzing a temporal sequence of light intensities that are recorded at specified pixels over time. By contrast, our rolling-shutter VLC mechanism is compatible with a wide range of inexpensive cameras on the market, such as smartphone cameras.

B. Visual-inertial Localization with Global Measurements

Map-based visual-inertial localization is an active research topic. Many [10]–[14] exploit visual feature-based maps where 3D landmarks are associated with image feature descriptors. The initial camera pose can be computed from 2D-3D matches between newly detected features and mapped landmarks. Next, accurate drift-free visual-inertial pose tracking can be done with subsequent map constraints. For example, [10] shows impressive efficiency and accuracy on mobile devices. However, such methods are likely to face robustness problems due to appearance changes, e.g., from illumination and weather. To alleviate such difficulties, recent works [18], [19] prefer using 3D LiDAR maps, which can provide accurate and stable representations of the environment's geometric information. However, they need external pose guesses as input at system

startup. In addition, real-time processing of LiDAR maps can cause considerable computational and memory burdens [18].

Many studies resort to artificial global pose measurements. In outdoor applications, GPS is being widely used to offer absolute position and Doppler velocity measurements relative to Earth. The fusion of VIO and GPS measurements can be performed in filtering- [20], [21] or graph optimization-based [22]–[24] frameworks. Compared to map-based solutions, such methods can provide satisfactory positioning accuracy and better computational efficiency. They are hence more suitable to run on resource-constrained platforms.

In this work, instead of using visual- or LiDAR-based map constraints, we utilize modulated LEDs as a kind of indoor *GPS* infrastructure to provide absolute pose measurements in a lightweight manner. Here VLC enables fast and reliable data association similar to GPS ranging messages. Also, different from traditional VLP systems, we exploit both modulated and unmodulated lights as location landmarks, thereby minimizing the additional infrastructure cost. We note that natural features are unusable here since our camera is heavily underexposed.

III. System Overview

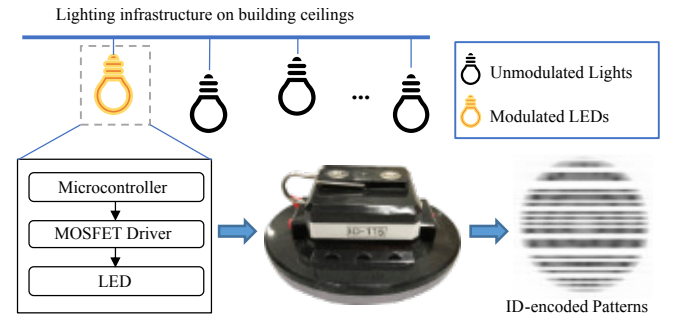

(a) Illustration of the lighting infrastructure for localization.

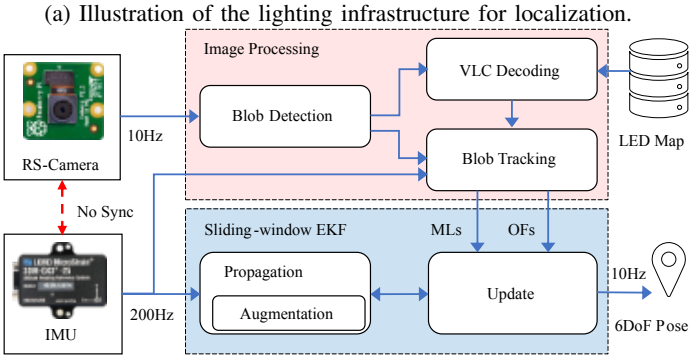

(b) Block diagram showing the workflow of our proposed method.

Fig. 1: Overall architecture of the proposed localization system.

The proposed system relies on ceiling lights in buildings for localization, as illustrated in Fig. 1a. Specifically, we replace a proportion of them with modulated LEDs as location beacons. The modulated LEDs broadcast unique identity codes through VLC. We adopt the exact VLC protocol as in our previous work [38], which runs on-off keying (OOK) modulation and Manchester coding. For experimentation, we made dozens of modulated LEDs using commercial off-the-shelf components. The sensor suite comprises a rolling-shutter (RS-) camera and a MEMS IMU without hardware synchronization between each other (see Fig. 1b). This sensor setup is common in low-cost consumer electronics. The rolling-shutter effect can cause motion blurs and distortions and hence contaminate regular vision-based pose estimation. However, in our case, it renders the camera a functional VLC receiver. We purposely exploit such a camera for VLC and taking visual measurements. The detailed VLC mechanism with rolling-shutter cameras is given in our supplementary material [58]. We note that successful decoding in the rolling-shutter VLC mechanism often requires a sufficiently large LED image, which carries at least a complete data packet. This causes inherent limitations to the decoding range and the number of decodable LEDs (i.e., MLs) per frame. In particular, the maximum decoding range is affected by the hardware and software configurations [38], such as the LED's modulation frequency and radiation surface size, the camera's rolling-shutter frequency and focal length, and the data packet length in the designed VLC protocol.

As shown in Fig. 1b, the image processing frontend extracts two types of blob features (i.e., MLs and OFs) from lights, feeding the EKF estimator. Light blobs are detected on incoming images and are tracked over frames until getting lost. We perform VLC decoding on certain blobs of modulated LEDs. If successfully decoded, the LED blobs can get their unique IDs and, from the prior map, the global 3D positions. They work as MLs to provide absolute pose measurements. Subject to the maximum VLC decoding range, some modulated LEDs at faraway locations are likely to suffer from decoding failures on individual images. Assisted by the short-term data association from blob tracking, we still have a chance to determine their LED IDs (i.e., for long-term data associations) later as the camera moves closer. The delayed data association leads to delayed ML measurements, which means they must be processed later, not immediately after their imaging times. This is very different from [38], in which MLs are always produced upon the arrival of a new image, and if valid, are immediately fed into a standard EKF for updates. On the other hand, the tracked blobs from unmodulated lights serve as OFs, providing relative geometric constraints. We note that even assisted by blob tracking, some modulated LEDs (e.g., too far away) cannot be decoded until their tracking is lost. In this case, we reuse them as OFs too. Hence, OFs can come from both unmodulated lights and undecoded LEDs.

To process these visual features and IMU measurements, we follow the stochastic cloning sliding window EKF framework in MSCKF (multi-state constraint Kalman filter) VIO [2]–[5]. Note blob tracking in the visual frontend introduces excessive delays to ML measurements, which cannot be properly handled by a standard EKF as it only keeps the current evolving state. In comparison, the stochastic cloning sliding window EKF further maintains a few clones of the previous state (or part thereof) in the sliding window. It can naturally incorporate delayed measurements like MLs. To process OFs, we leverage the multi-state constraint measurement model by MSCKF [2]. Following this, OF measurements are quickly marginalized via nullspace projection, imposing motion constraints on multiple cloned camera/IMU poses in the state vector. This avoids the burden of adding OFs to the state vector and allows efficient EKF updates. IMU measurements are used to propagate the

state vector and covariance matrix. When a new image arrives, the filter is augmented with a clone of the current IMU pose estimate. Once the sliding window becomes full, the oldest IMU pose will be marginalized to keep bounded computation. We perform EKF updates when a processed ML/OF feature track becomes available or if the oldest IMU pose before marginalization has associated valid ML measurements. An overview of our algorithm flow is given in Algorithm 1.

Algorithm 1

Image registration: When a new image is recorded,

- detect and track light blobs and optionally do VLC decoding (cf. Section IV).
  - produce ML measurements from modulated LEDs that are registered a priori and successfully decoded.
  - produce OF measurements from other lights, either unmodulated or undecoded.
- augment the state vector and covariance matrix with a clone of the current IMU pose estimate (cf. Section V-B).

Propagation: Propagate the state vector and covariance matrix using IMU measurements received between two consecutive imaging times (cf. Section V-B).

EKF update: Process any MLs or OFs available (cf. Section V-D),

- when blob tracks are lost,
  - if MLs exist in the lost tracks, perform a map-based update according to Eq. 20 with all the associated MLs;
  - perform an MSCKF-based update according to Eq. 22 with all the lost OFs that have been tracked for multiple frames.
- when the sliding window is full,
  - if the oldest IMU pose is associated with MLs, perform a map-based update according to Eq. 20 with these MLs;
  - remove this pose from the state vector, modify the related covariance matrix, and discard any associated OFs.

IV. Image Processing

In this section, we detail the three modules of the image processing frontend in the proposed system, including blob detection in Section IV-A, blob tracking in Section IV-B, and VLC decoding in Section IV-C. Note the blob detection and VLC decoding methods are mostly repeated from those in our previous work [38], while the blob tracking method is built on well-developed techniques in the literature. These modules per se are hence not the contribution of this work. The related content is listed for the sake of completeness. However, our use of blob tracking to assist VLC decoding is novel in the VLP context, as explained in Section IV-C.

A. Blob Detection

To facilitate VLC, the camera needs to capture images with a very short exposure time [33]–[35]. Therefore, natural visual features in the surroundings are hard to detect, while bright objects (e.g., light bulbs) can be easily distinguished. We are interested in blobs of high intensities. This region-of-interest (ROI) can correspond to lit lights, modulated or unmodulated. First, the input grayscale image is binarized with a fixed threshold[2] (e.g., 20 in our implementation). Images of unmodulated lights are solid blobs with locally consistent intensities. Finding such blobs in a binary image is straightforward with the standard blob detection technique. However, for modulated LEDs, the rolling-shutter effect should be considered.

The modulated LED with fast-changing intensities yields parallel strip patterns inside its ROI due to rolling shutter effect [33]–[35]. As illustrated in Fig. 1a, the patterns are comprised of dark and bright strips that interleave across rows. It is desired to join all the foreground pixels (e.g., bright strips) into a single connected blob. We perform vertical dilation on the binary image to fill in dark gaps. After this, candidate blobs are detected in the dilated image. Small blobs[3] are filtered out to suppress image noises and remove ambient bright patches that are less likely to be stably tracked. For each of the remaining blobs, we compute the centroid pixel coordinates[4], $\mathbf{p} = (u, v)$, and the radius of its minimum enclosing circle in pixels, r, and create a bounding box as the ROI mask. We crop the grayscale image within this mask and associate each cropped grayscale patch, $\mathcal{I}$, to the respective blob. We describe it using a tuple $\mathcal{B} = (\mathrm{TID}, \mathrm{PID}, \mathbf{p}, r, \mathcal{I})$, where TID is its temporal feature ID for short-term data associations, and PID is the permanent LED ID for modulated LEDs. Fig. 2 illustrates the key steps.

From each image, we obtain a set of blob features $\mathcal{S} = \{\mathcal{B}_i\}$, $i = 1, \cdots, n_S$. These will be tracked over consecutive frames, and if possible, decoded by the VLC decoder.

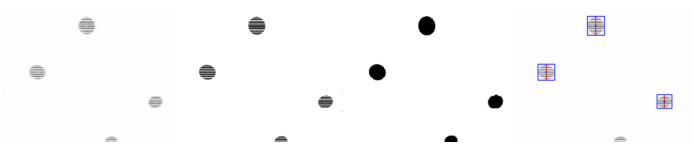

(a) Grayscale (b) Binarized (c) Dilated (d) Detected

Fig. 2: Illustration of the blob detection process. We show inverted images for better visualization on paper.

B. Blob Tracking

We try to detect blobs on the current image and find their best matches in the previous frame. The appearance of lights is not informative to help disambiguate individual blobs, as lights in a neighboring area often have the same form factor. The appearance of modulated LEDs even changes over time due to their asynchronous communications to the camera. We resort to finding the nearest neighbors with spatial coherence.

We consider two sets of blobs, $\mathcal{S}_k$ and $\mathcal{S}_{k+1}$, detected from two sequential camera frames, $\{C_k\}$ and $\{C_{k+1}\}$, respectively. For each pair of blobs, $\mathcal{B}_i \in \mathcal{S}_k$ and $\mathcal{B}_j \in \mathcal{S}_{k+1}$, we define a cost function describing the overlap between their minimum enclosing circles, i.e.,

$$c(\mathcal{B}_i, \mathcal{B}_j) = \|\mathbf{p}_j - \mathbf{p}_i\| / |r_i + r_j|. \tag{1}$$

[2]In our experiments, using a fixed threshold gives satisfying results at low computational cost. However, if the light's intensity changes greatly from our existing settings, adaptive thresholding like Otsu's method is a better choice.

[3]In our case, the image resolution is 1640×1232, and the ceiling height is about 2.3 m. Small blobs are discarded whose height is less than 40 pixels.

[4]We approximate the blob centroid as the image of the corresponding light's centroid. In later state estimation, we accommodate this approximation error by inflating the measurement noise of blob features.

We assume that the mutual distance of blobs in an image frame is greater than the respective inter-frame pixel displacement. In our context, the assumption works well in practice, owing to the inherent sparsity of ceiling lights and the non-rapid camera motion. This can be expected for pedestrians or low-speed service robots. Rotational movements are more likely to yield large pixel displacements between two sequential frames, violating the above assumption. To relax this issue, we predict the centroid location, $\mathbf{p}'_i$, of the blob $\mathcal{B}_i$ observed from $\{C_k\}$ in the next frame $\{C_{k+1}\}$ using IMU measurements. The camera's rotational change, ${}^{C_{k+1}}_{C_k}\mathbf{R}$, can be obtained by integrating gyroscope measurements from time step k to $k+1$. Neglecting the inter-frame translation and camera distortion, according to [59], we have the approximate relation as follows:

$$\begin{bmatrix}\mathbf{p}'_i\\ 1\end{bmatrix} = \mathbf{K}\,{}^{C_{k+1}}_{C_k}\mathbf{R}\mathbf{K}^{-1}\begin{bmatrix}\mathbf{p}_i\\ 1\end{bmatrix}, \tag{2}$$

where $\mathbf{K}$ is the known camera intrinsic matrix; and $\mathbf{p}_i$ and $\mathbf{p}'_i$ are the original and predicted blob centroids in pixels, respectively. In addition, we expect a small perspective distortion in a short frame transition time and set the predicted blob radius as $r'_i = r_i$. After this, we modify the cost function $c(\mathcal{B}_i, \mathcal{B}_j)$ in Eq. 1 as $c'(\mathcal{B}_i, \mathcal{B}_j) = \|\mathbf{p}_j - \mathbf{p}'_i\|/|r_i + r_j|$, where $\mathbf{p}'_i$ is computed from Eq. 2. Accordingly, the cost matrix is created:

$$\mathbf{C}(\mathcal{S}_k, \mathcal{S}_{k+1}) = [c'(\mathcal{B}_i, \mathcal{B}_j)]_{\mathcal{B}_i\in\mathcal{S}_k, \mathcal{B}_j\in\mathcal{S}_{k+1}}, \tag{3}$$

where the element at row i and column j represents the cost between the previous blob $\mathcal{B}_i$ and the current blob $\mathcal{B}_j$.

We find newly detected blobs in $\mathcal{S}_{k+1}$ by examining the cost matrix $\mathbf{C}$. For each $\mathcal{B}_j \in \mathcal{S}_{k+1}$, if all entries in the column $\mathbf{C}_j$ exceed a predefined threshold (e.g., 5 in our implementation), we treat it as a new blob and create a new TID for it. $\mathcal{B}_j$ is then removed from $\mathcal{S}_{k+1}$. The affected column of the cost matrix is also removed. Next, the goal is to find an assignment of the remaining blobs in $\mathcal{S}_{k+1}$ to the previous blobs in $\mathcal{S}_k$ such that the total cost is minimal. This *assignment problem* can be optimally solved by the Hungarian method in polynomial time [60]. The TID remains unchanged for tracked blobs.

We keep track of light blobs until they are not visible anymore. Finally, we obtain a set of blob tracks $\{\mathcal{T}_i\}$, $i = 1, \cdots, n_T$ for n_T lights. $\mathcal{T}_i$ is an ordered list of blobs, $\langle \mathcal{B}_1, \cdots, \mathcal{B}_{n_i}\rangle$, observed from n_i consecutive frames. In particular, each track belonging to modulated LEDs will have a valid PID upon successful VLC decoding. With the short-term data association, blobs that are part of the track have the same PID, thus being identifiable once any one is decodable.

C. VLC Decoding

The time-varying light signals from LEDs are perceived by the rolling-shutter camera as spatially-varying strip patterns. We intend to retrieve the encoded VLC messages from such barcode-like patterns. Let us consider a set of blobs detected from a given camera frame, $\mathcal{S} = \{\mathcal{B}_i\}$, $i = 1, \cdots, n_S$.

Blobs with barcode-like strip patterns correspond to modulated LEDs. We aim to retrieve the encoded VLC information from the induced dark and bright strips of varying widths. Note that the VLC packet is decodable only if the blob is large enough to contain a complete data packet [38]. Therefore, blobs whose sizes are smaller than a given threshold (e.g., 80 pixels in height in our implementation) will be culled in this step. For each remaining blob $\mathcal{B}_i$, we pick up grayscale pixels in the centering column of the associated image patch $\mathcal{I}_i$. Knowing the camera's sampling frequency, we treat these row-indexed pixel values as a time-varying 1D signal. It is then binarized by adaptive thresholding [61] to account for the non-uniform illumination artifact of the light's radiation surface. Fig. 3 shows an example of 1D signals before and after binarization. To recover VLC information from the binary waveform, we use a state machine-based method for OOK demodulation and Manchester decoding. We can then obtain the LED's ID from the decoding result and assign it to the PID of the corresponding blob feature.

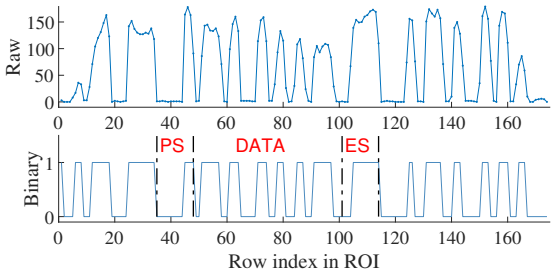

Fig. 3: Example of the 1D intensity signal for VLC decoding. The raw signal comprises the grayscale pixels in the center column of an ROI. The segments of the binary signal (marked with the following symbols: PS, DATA, and ES) constitute a complete data packet.

Owing to the blob tracking, the PID is shared among all the tracked blobs. As a result, LED blobs that cannot be decoded at faraway locations still have a chance to be identified later as the camera approaches, until their tracking gets lost. This gives more detection instances of decoded LEDs (i.e., MLs). In this sense, the overall decoding performance during camera motion can be improved. Due to asynchronous LED-to-camera communications, the received data packet may start randomly in the ROI. For small blobs that contain a single complete packet, it is possible that only shifted signal waveforms exist. To mitigate this issue, we adopt a bidirectional decoding scheme as in [35] that allows greater success in such cases. For some larger blobs, we decode all the repeating packets inside and crosscheck the results for consistency. Errors could happen due to the lack of dedicated data integrity checking in our simplified VLC protocol. Hence, the pose estimator should be resilient to occasional communication errors.

V. Estimator Description

Notations: We define a fixed global reference frame, $\{G\}$, which is gravity aligned and with its z-axis pointing upwards to the ceiling. We denote the IMU body frame as $\{I\}$ and the camera frame as $\{C\}$. We use the unit quaternion ${}^A_B\bar{\mathbf{q}}$ under JPL convention [62] to represent the rotation ${}^A_B\mathbf{R}$ from frame $\{B\}$ to $\{A\}$, i.e., ${}^A_B\mathbf{R} = \mathbf{R}\left({}^A_B\bar{\mathbf{q}}\right)$. The symbol $\otimes$ is used to denote quaternion multiplication. For a quantity $\mathbf{a}$, we use $\hat{\mathbf{a}}$ for its estimate and $\tilde{\mathbf{a}}$ for the residue.

For the estimator description, we follow the conventions and general formulations established in MSCKF [2]–[5]. In

what follows, we show in detail the EKF estimator, including state vector in Section V-A, IMU dynamics, state propagation and augmentation in Section V-B, rolling-shutter camera measurement model in Section V-C, and EKF update with MLs/OFs in Section V-D. The equations of the estimator are inherited from [2]–[5], [63] and are not the contribution of this work. Instead, the involved technical novelties are within the VLP context and attributed to the additional use of delayed ML measurements and the novel use of unmodulated lights as OFs to provide motion constraints for VLP. The benefits of these design choices are discussed previously in Section II and Section III, and we will further explain how to achieve this in Section V-D. The standard parts of MSCKF are presented for greater completeness of the system description, thus providing the reader with a better understanding.

A. State Vector

At imaging time-step, k, the state vector, $\mathbf{x}_k$, maintains the current IMU state, $\mathbf{x}_I$, and in the sliding window, clones of m past IMU poses, $\mathbf{x}_C$, i.e., $\mathbf{x}_k = \begin{bmatrix}\mathbf{x}_I^\top & \mathbf{x}_C^\top\end{bmatrix}^\top$, as in [2]–[5], [63]. The cloned poses correspond to the latest m imaging times.

The explicit forms of $\mathbf{x}_I$ and $\mathbf{x}_C$ are given by

$$\mathbf{x}_I = \begin{bmatrix} {}^{I_k}_{G}\bar{\mathbf{q}}^\top & {}^G\mathbf{p}_{I_k}^\top & {}^G\mathbf{v}_{I_k}^\top & \mathbf{b}_g^\top & \mathbf{b}_a^\top & {}^C_I\bar{\mathbf{q}}^\top & {}^C\mathbf{p}_I^\top & t_d & t_r \end{bmatrix}^\top \quad (4)$$

$$\mathbf{x}_C = \begin{bmatrix} {}^{I_{k-1}}_{G}\bar{\mathbf{q}}^\top & {}^G\mathbf{p}_{I_{k-1}}^\top & \cdots & {}^{I_{k-m}}_{G}\bar{\mathbf{q}}^\top & {}^G\mathbf{p}_{I_{k-m}}^\top \end{bmatrix}^\top, \quad (5)$$

where ${}^{I_k}_{G}\bar{\mathbf{q}}$ is the unit quaternion that describes the rotation, ${}^{I_k}_{G}\mathbf{R}$, from the global frame to the IMU frame. ${}^G\mathbf{p}_{I_k}$ and ${}^G\mathbf{v}_{I_k}$ is the respective position and velocity of the IMU expressed in the global frame. $\mathbf{b}_g$ and $\mathbf{b}_a$ represents the underlying bias for the gyroscope and accelerometer readings, respectively. ${}^C_I\bar{\mathbf{q}}$ is the unit quaternion describing the rotation, ${}^C_I\mathbf{R}$, from the IMU frame to the camera frame. ${}^C\mathbf{p}_I$ is the translation of the IMU with respect to the camera frame. The scalar t_d is the time offset between these two sensors. t_r is the frame readout time of the rolling-shutter camera. The vector $\mathbf{x}_C$ comprises the m latest IMU pose clones, i.e., ${}^{I_{k-i}}_{G}\bar{\mathbf{q}}$ and ${}^G\mathbf{p}_{I_{k-i}}$, $i = 1, \ldots, m$.

Following [4], [5], we include in the filter state the IMU-camera spatial extrinsics, $\{{}^C_I\bar{\mathbf{q}}, {}^C\mathbf{p}_I\}$. The system can hence accommodate certain offline calibration inaccuracies. Due to the lack of hardware synchronization in our sensor suite, we estimate the IMU-camera time offset, t_d, as in [4]. Also, it is useful to estimate the rolling-shutter frame readout time t_r online, if not given by the camera's datasheet. For t_d, we use the IMU clock as the time reference and model it by a small unknown constant [4]. The *true* imaging time for an image with a camera timestamp, ${}^Ct_k$, is given by ${}^It_k = {}^Ct_k + t_d$. To estimate t_r, we follow the method proposed in [63].

The error-state vector for $\mathbf{x}_I$ is defined as

$$\tilde{\mathbf{x}}_I = \begin{bmatrix} {}^G\tilde{\boldsymbol{\theta}}_{I_k}^\top & {}^G\tilde{\mathbf{p}}_{I_k}^\top & {}^G\tilde{\mathbf{v}}_{I_k}^\top & \tilde{\mathbf{b}}_g^\top & \tilde{\mathbf{b}}_a^\top & {}^I\tilde{\boldsymbol{\phi}}^\top & {}^C\tilde{\mathbf{p}}_I^\top & \tilde{t}_d & \tilde{t}_r \end{bmatrix}^\top, \quad (6)$$

where standard additive errors apply to vector quantities (e.g., $\mathbf{p} = \hat{\mathbf{p}} + \tilde{\mathbf{p}}$) and multiplicative errors apply to quaternions, as in [2]–[5], [63]. We follow the global quaternion error definition [3] for the IMU orientation and have ${}^I_G\bar{\mathbf{q}} \simeq {}^I_G\hat{\bar{\mathbf{q}}} \otimes \begin{bmatrix}\frac{1}{2}{}^G\tilde{\boldsymbol{\theta}}^\top & 1\end{bmatrix}^\top$, where the 3×1 vector ${}^G\tilde{\boldsymbol{\theta}}$ is a minimal representation of the angle errors defined in $\{G\}$. For ${}^C_I\bar{\mathbf{q}}$, as in [4], [5], we have ${}^C_I\bar{\mathbf{q}} \simeq {}^C_I\hat{\bar{\mathbf{q}}} \otimes \begin{bmatrix}\frac{1}{2}{}^I\tilde{\boldsymbol{\phi}}^\top & 1\end{bmatrix}^\top$, where ${}^I\tilde{\boldsymbol{\phi}}$ is the 3×1 angle-error vector defined in $\{I\}$.

Accordingly, the error-state vector for the full state $\mathbf{x}_k$ is

$$\tilde{\mathbf{x}}_k = \begin{bmatrix} \tilde{\mathbf{x}}_I^\top \mid {}^G\tilde{\boldsymbol{\theta}}_{I_{k-1}}^\top & {}^G\tilde{\mathbf{p}}_{I_{k-1}}^\top & \cdots & {}^G\tilde{\boldsymbol{\theta}}_{I_{k-m}}^\top & {}^G\tilde{\mathbf{p}}_{I_{k-m}}^\top \end{bmatrix}^\top. \quad (7)$$

The corresponding covariance matrix, $\mathbf{P}_{k|k}$, is partitioned as

$$\mathbf{P}_{k|k} = \begin{bmatrix} \mathbf{P}_{II_{k|k}} & \mathbf{P}_{IC_{k|k}} \\ \mathbf{P}_{IC_{k|k}}^\top & \mathbf{P}_{CC_{k|k}} \end{bmatrix}, \quad (8)$$

where $\mathbf{P}_{II_{k|k}}$ and $\mathbf{P}_{CC_{k|k}}$ denotes the covariance of the current IMU state and the past IMU poses, respectively, and $\mathbf{P}_{IC_{k|k}}$ represents the cross-correlation between their estimate errors.

B. State Propagation and Augmentation

Following [3]–[5], the IMU measurements, $\boldsymbol{\omega}_m$ and $\mathbf{a}_m$, are related to the true angular velocity, ${}^I\boldsymbol{\omega}$, and linear acceleration, ${}^I\mathbf{a}$, in the local IMU frame by the sensor model:

$$\boldsymbol{\omega}_m = {}^I\boldsymbol{\omega} + \mathbf{b}_g + \mathbf{n}_g,\ \mathbf{a}_m = {}^I\mathbf{a} - {}^I_G\mathbf{R}\,{}^G\mathbf{g} + \mathbf{b}_a + \mathbf{n}_a, \quad (9)$$

where ${}^G\mathbf{g} = [0,\ 0,\ -9.8\,m/s^2]$ is the gravity vector expressed in $\{G\}$; and $\mathbf{n}_g$ and $\mathbf{n}_a$ are zero-mean white Gaussian noise.

Like in [3]–[5], the continuous-time process model for $\mathbf{x}_I$ is described by

$$\begin{aligned} &{}^I_G\dot{\bar{\mathbf{q}}} = \frac{1}{2}\boldsymbol{\Omega}\left({}^I\boldsymbol{\omega}\right){}^I_G\bar{\mathbf{q}},\ {}^G\dot{\mathbf{p}}_I = {}^G\mathbf{v}_I,\ {}^G\dot{\mathbf{v}}_I = {}^I_G\mathbf{R}^\top{}^I\mathbf{a}, \\ &\dot{\mathbf{b}}_g = \mathbf{n}_{wg},\ \dot{\mathbf{b}}_a = \mathbf{n}_{wa},\ {}^C_I\dot{\bar{\mathbf{q}}} = \mathbf{0},\ {}^C\dot{\mathbf{p}}_I = \mathbf{0},\ \dot{t}_d = 0,\ \dot{t}_r = 0, \end{aligned} \quad (10)$$

where $\boldsymbol{\Omega}(\boldsymbol{\omega}) = \begin{bmatrix} -\lfloor\boldsymbol{\omega}_\times\rfloor & \boldsymbol{\omega} \\ -\boldsymbol{\omega}^\top & 0 \end{bmatrix}$. The operator $\lfloor\cdot_\times\rfloor$ denotes the skew-symmetric matrix. $\mathbf{n}_{wg}$ and $\mathbf{n}_{wa}$ are the zero-mean white Gaussian noise processes driving the IMU biases.

With the expectation of Eq. 10, we propagate the nominal IMU state $\hat{\mathbf{x}}_I$ by numerical integration using buffered IMU measurements. The estimates of cloned IMU poses in the sliding window, $\hat{\mathbf{x}}_C$, are constant during this propagation.

To propagate the covariance, as in [2], we begin with the linearized continuous-time IMU error-state equation:

$$\dot{\tilde{\mathbf{x}}}_I = \mathbf{F}_I\,\tilde{\mathbf{x}}_I + \mathbf{G}_I\,\mathbf{n}_I, \quad (11)$$

where $\mathbf{n}_I = \begin{bmatrix}\mathbf{n}_g^\top & \mathbf{n}_{wg}^\top & \mathbf{n}_a^\top & \mathbf{n}_{wa}^\top\end{bmatrix}^\top$ is the process noise modeled by a Gaussian process with autocorrelation $\mathbb{E}[\mathbf{n}_I(t)\mathbf{n}_I^\top(\tau)] = \mathbf{Q}_c\,\delta(t-\tau)$. $\mathbf{Q}_c = \mathrm{diag}\{\sigma_g^2\mathbf{I}_3, \sigma_{wg}^2\mathbf{I}_3, \sigma_a^2\mathbf{I}_3, \sigma_{wa}^2\mathbf{I}_3\}$ is the covariance of the continuous-time system noise that depends on the IMU noise characteristics [1]. $\mathbf{F}_I$ and $\mathbf{G}_I$ are Jacobians with respect to the IMU state error and the process noise. The detailed expressions of $\mathbf{F}_I$ and $\mathbf{G}_I$ are given in the supplementary material [58].

Given a new arriving IMU measurement at τ_{k+1}, we can propagate the covariance for the IMU error state, $\mathbf{P}_{II_{k|k}}$, one step forward from the previous IMU sampling time τ_k to τ_{k+1}. To this end, we compute the discrete-time system transition matrix, $\boldsymbol{\Phi}_{k+1,k}$, and the noise covariance, $\mathbf{Q}_k$, for Eq.11:

$$\boldsymbol{\Phi}_{k+1,k} \simeq \exp\left(\mathbf{F}_I(\tau_k)\Delta t\right),\ \mathbf{Q}_k \simeq \mathbf{G}_I(\tau_k)\mathbf{Q}_c\mathbf{G}_I^\top(\tau_k)\Delta t,$$

where we assume $\mathbf{F}_I$ is constant over the small interval, $\Delta t = \tau_{k+1} - \tau_k$. The propagated covariance $\mathbf{P}_{II_{k+1|k}}$ is given by

$$\mathbf{P}_{II_{k+1|k}} = \mathbf{\Phi}_{k+1,k}\mathbf{P}_{II_{k|k}}\mathbf{\Phi}_{k+1,k}^\top + \mathbf{Q}_k. \tag{12}$$

The covariance matrix of the cloned poses, $\mathbf{P}_{CC_{k|k}}$, does not change, but the cross-correlation matrix $\mathbf{P}_{IC_{k|k}}$ is affected. The covariance matrix for the full state is propagated as

$$\mathbf{P}_{k+1|k} = \begin{bmatrix} \mathbf{P}_{II_{k+1|k}} & \mathbf{\Phi}_{k+1,k}\mathbf{P}_{IC_{k|k}} \\ \mathbf{P}_{IC_{k|k}}^\top\mathbf{\Phi}_{k+1,k}^\top & \mathbf{P}_{CC_{k|k}} \end{bmatrix}. \tag{13}$$

When a new image arrives, the state vector and covariance will be augmented to incorporate the corresponding IMU pose [2]–[5], [63]. Let us consider an image with timestamp t. By our definition, its true measurement time is $t + t_d$. Ideally, we need to augment the state with an estimate of the current IMU pose at time $t + t_d$. In practice, we propagate the EKF state and the covariance up to $t + \hat{t}_d$, the best estimate we have for the true imaging time [4], using buffered IMU measurements. After that, a clone of the latest IMU pose estimate $[{}^I_G\hat{\bar{\mathbf{q}}}^\top(t + \hat{t}_d)\ {}^G\hat{\mathbf{p}}_I^\top(t + \hat{t}_d)]^\top$ is appended to the state vector. Also, the covariance matrix is augmented to include the covariance of the newly cloned state, as well as its correlation with the old state. The augmented system covariance matrix is given by

$$\mathbf{P}_{k+1|k} \leftarrow \begin{bmatrix} \mathbf{P}_{k+1|k} & \mathbf{P}_{k+1|k}\mathbf{J}_a^\top \\ \mathbf{J}_a\mathbf{P}_{k+1|k} & \mathbf{J}_a\mathbf{P}_{k+1|k}\mathbf{J}_a^\top \end{bmatrix}, \tag{14}$$

with $\mathbf{J}_a = \begin{bmatrix}\mathbf{I}_{6\times 6}\ \mathbf{0}_{6\times(17+6m)}\end{bmatrix}$, where m is the number of previously cloned poses in the sliding window.

C. Rolling-shutter Camera Model

To deal with rolling-shutter camera measurements for state estimation properly, we follow the rolling-shutter measurement model in [63]. Rolling shutters capture N rows on an image sequentially at varying times. Following the convention in [63], we treat imaging time for a rolling-shutter camera as the time instance when the middle row is captured. Given an image timestamped at t, the true sampling time (e.g., corresponding to the middle row) is $t + t_d$ by the IMU clock. The nth row away from the middle is captured at $t_n = t + t_d + n\frac{t_r}{N}$, where $n \in (-\frac{N}{2}, \frac{N}{2}]$ and t_r is the frame readout time. For a moving camera, individual rows on one image may correspond to varying camera poses.

Let us consider the ith feature, f_i, detected by the frontend. Without loss of generality, we suppose the feature's pixel observation from the jth cloned pose, $\mathbf{z}_{ij}$, lies in the nth row. Assuming a calibrated pinhole camera model, we have

$$\begin{aligned} \mathbf{z}_{ij} &= \mathbf{h}\left({}^{C_j}\mathbf{p}_{f_i}(t_n)\right) + \mathbf{n}_{ij} \\ {}^{C_j}\mathbf{p}_{f_i}(t_n) &= {}^C_I\mathbf{R}\,{}^{I_j}_G\mathbf{R}(t_n)\left({}^G\mathbf{p}_{f_i} - {}^G\mathbf{p}_{I_j}(t_n)\right) + {}^C\mathbf{p}_I, \end{aligned} \tag{15}$$

where $\mathbf{h}(\cdot)$ is the perspective projection, i.e., $\mathbf{h}\left([x,y,z]^\top\right) = [x/z, y/z]^\top$. ${}^{C_j}\mathbf{p}_{f_i}$ is the feature position in the camera frame that relates to the jth IMU pose. $\mathbf{n}_{ij}$ is the normalized image measurement noise. ${}^G\mathbf{p}_{f_i}$ is the global 3D feature position. This can be obtained in different ways according to the feature types. For MLs, the feature position is known directly from the registered LED map by VLC. For OFs, the feature position will be triangulated using the tracked feature measurements and cloned IMU poses in the sliding window, as in [2].

The linearized residue, $\mathbf{r}_{ij} = \mathbf{z}_{ij} - \hat{\mathbf{z}}_{ij}$, at time $\hat{t}_n$ is

$$\begin{aligned} \mathbf{r}_{ij} \simeq& \mathbf{H}_\theta^{ij}(\hat{t}_n)\,{}^G\tilde{\boldsymbol{\theta}}_{I_j}(\hat{t}_n) + \mathbf{H}_{\mathbf{p}}^{ij}(\hat{t}_n)\,{}^G\tilde{\mathbf{p}}_{I_j}(\hat{t}_n) + \\ & \mathbf{H}_{\mathbf{x}_I}^{ij}(\hat{t}_n)\tilde{\mathbf{x}}_I + \mathbf{H}_f^{ij}(\hat{t}_n){}^G\tilde{\mathbf{p}}_{f_i} + \mathbf{n}_{ij}, \end{aligned} \tag{16}$$

where ${}^G\tilde{\boldsymbol{\theta}}_{I_j}(\hat{t}_n)$ and ${}^G\tilde{\mathbf{p}}_{I_j}(\hat{t}_n)$ are errors in the jth IMU pose, and ${}^G\tilde{\mathbf{p}}_{f_i}$ is the 3D feature position error. $\mathbf{H}_\theta^{ij}(\hat{t}_n)$ and $\mathbf{H}_{\mathbf{p}}^{ij}(\hat{t}_n)$ are Jacobians with respect to the jth IMU pose. $\mathbf{H}_{\mathbf{x}_I}^{ij}(\hat{t}_n)$ and $\mathbf{H}_f^{ij}(\hat{t}_n)$ is the Jacobian for the current IMU state and the global feature position, respectively. The explicit expressions of these Jacobians are given in the supplementary material [58]. ${}^G\tilde{\boldsymbol{\theta}}_{I_j}(\hat{t}_n)$ and ${}^G\tilde{\mathbf{p}}_{I_j}(\hat{t}_n)$ depend on time $\hat{t}_n$ and do not exist in the filter's error state. Remember that, as in [63], we have only cloned the IMU pose at time $t + \hat{t}_d$ to the filter during state augmentation. As a result, it can not be used for EKF updates directly. By taking the Taylor expansion at $t + \hat{t}_d$, we approximate these pose errors by the resulting zeroth-order terms for computational efficiency [63]. Explicitly, we have ${}^G\tilde{\boldsymbol{\theta}}_{I_j}(\hat{t}_n) \approx {}^G\tilde{\boldsymbol{\theta}}_{I_j}(t + \hat{t}_d)$ and ${}^G\tilde{\mathbf{p}}_{I_j}(\hat{t}_n) \approx {}^G\tilde{\mathbf{p}}_{I_j}(t + \hat{t}_d)$. Accordingly, the residue is rewritten as

$$\begin{aligned} \mathbf{r}_{ij} \simeq& \mathbf{H}_\theta^{ij}\,{}^G\tilde{\boldsymbol{\theta}}_{I_j}(t + \hat{t}_d) + \mathbf{H}_{\mathbf{p}}^{ij}\,{}^G\tilde{\mathbf{p}}_{I_j}(t + \hat{t}_d) + \\ & \mathbf{H}_{\mathbf{x}_I}^{ij}\tilde{\mathbf{x}}_I + \mathbf{H}_f^{ij}{}^G\tilde{\mathbf{p}}_{f_i} + \mathbf{n}_{ij} \\ =& \mathbf{H}_{\mathbf{x}}^{ij}\tilde{\mathbf{x}} + \mathbf{H}_f^{ij}{}^G\tilde{\mathbf{p}}_{f_i} + \mathbf{n}_{ij}, \end{aligned} \tag{17}$$

where $\mathbf{H}_{\mathbf{x}}^{ij} = \begin{bmatrix}\mathbf{H}_{\mathbf{x}_I}^{ij}\ \mathbf{0}_{2\times 6}\ \cdots\ \mathbf{H}_\theta^{ij}\ \mathbf{H}_{\mathbf{p}}^{ij}\ \cdots\ \mathbf{0}_{2\times 6}\end{bmatrix}$ represents the Jacobian with respect to the full filter state, and the time variables in these Jacobians are omitted for brevity.

Suppose feature f_i has been tracked from a set of M_i poses. We compute the residues and Jacobians for all observations to this feature and obtain its stacked residue form as follows:

$$\mathbf{r}_i \simeq \mathbf{H}_{\mathbf{x}}^i\tilde{\mathbf{x}} + \mathbf{H}_{f_i}{}^G\tilde{\mathbf{p}}_{f_i} + \mathbf{n}_i, \tag{18}$$

where $\mathbf{r}_i$, $\mathbf{H}_{\mathbf{x}}^i$, $\mathbf{H}_{f_i}$ and $\mathbf{n}_i$ are block vectors or matrices. $\mathbf{n}_i$ is the normalized image noise vector with covariance $\sigma_{\text{im}}^2\mathbf{I}_{2M_i}$. In our implementation, we empirically set a conservative value for σ_{im} to accommodate some approximation errors that arise from the blob detection step (cf. Section IV-A). Eq. 18 is not ready for EKF updates because the feature position error, ${}^G\tilde{\mathbf{p}}_{f_i}$, is not in the filter error state. In what follows, we will describe how we mitigate this issue in Section V-D.

D. EKF Update

We present the residues for two types of blob features:

1) Residue for MLs: The global feature positions of MLs, ${}^G\mathbf{p}_{f_i}$, are known from the prior LED feature map. The affected errors, ${}^G\tilde{\mathbf{p}}_{f_i}$, are due to offline mapping and are independent of the filter error state, $\tilde{\mathbf{x}}$, in online estimation (cf. Eq. 18). As in [38], we model this error as zero-mean white Gaussian noise with covariance $\sigma_f^2\mathbf{I}_3$. Eq. 18 can be rewritten as

$$\mathbf{r}_i \simeq \mathbf{H}_{\mathbf{x}}^i\tilde{\mathbf{x}} + \mathbf{n}_i', \tag{19}$$

where $\mathbf{n}_i' = \mathbf{H}_{f_i}{}^G\tilde{\mathbf{p}}_{f_i} + \mathbf{n}_i$ denotes the inflated noise. It is Gaussian with covariance $\mathbb{E}\left(\mathbf{n}_i'\mathbf{n}_i'^\top\right) = \sigma_f^2\mathbf{H}_{f_i}\mathbf{H}_{f_i}^\top + \sigma_{\text{im}}^2\mathbf{I}_{2M_i}$. Once we have determined which MLs to process at a given

time, we compute their residues and Jacobians as per Eq. 19. Stacking them together yields the final residue for MLs:

$$\mathbf{r}_{\text{ML}} \simeq \mathbf{H}_{\text{ML}}\tilde{\mathbf{x}} + \mathbf{n}_{\text{ML}}, \tag{20}$$

where $\mathbf{r}_{\text{ML}}$ is a block vector with elements $\mathbf{r}_i$, $\mathbf{H}_{\text{ML}}$ is a block matrix with elements $\mathbf{H}_{\mathbf{x}}^i$, and $\mathbf{n}_{\text{ML}}$ is a block vector with elements $\mathbf{n}_i'$. To account for false data associations, e.g., due to errors in VLC decoding or blob tracking, only those elements passing the Mahalanobis gating test are retained. We can now use Eq. 20 for an EKF update with all valid MLs. We call this step a map-based update.

2) Residue for OFs: Following the standard MSCKF [2], the global feature positions of OFs are triangulated using the tracked features and cloned poses in the filter. The resulting errors, ${}^G\tilde{\mathbf{p}}_{f_i}$, are correlated to the error state, $\tilde{\mathbf{x}}$. To eliminate this correlation, the nullspace projection technique in MSCKF [2] is applied. Let $\mathbf{U}_i$ denote an unitary matrix whose columns span the left nullspace of $\mathbf{H}_{f_i}$, i.e., $\mathbf{U}_i^\top \mathbf{H}_{f_i} = \mathbf{0}$. Multiplying $\mathbf{U}_i^\top$ to Eq. 18 yields the following residue:

$$\mathbf{r}_i^o = \mathbf{U}_i^\top \mathbf{r}_i \simeq \mathbf{U}_i^\top \mathbf{H}_{\mathbf{x}}^i \tilde{\mathbf{x}} + \mathbf{U}_i^\top \mathbf{n}_i = \mathbf{H}_{\mathbf{x}}^{i,o}\tilde{\mathbf{x}} + \mathbf{n}_i^o, \tag{21}$$

where the covariance of the projected noise, $\mathbf{n}_i^o$, is $\sigma_{\text{im}}^2 \mathbf{I}_{2M_i-3}$. Likewise, we aggregate the residues and Jacobians for all OFs to be processed, as computed from Eq. 21, and pass them to a Mahalanobis gating test. The remaining elements constitute the final residue for OFs:

$$\mathbf{r}_{\text{OF}} \simeq \mathbf{H}_{\text{OF}}\tilde{\mathbf{x}} + \mathbf{n}_{\text{OF}}, \tag{22}$$

where $\mathbf{r}_{\text{OF}}$ is a block vector with elements $\mathbf{r}_i^o$, $\mathbf{H}_{\text{OF}}$ is a block matrix with elements $\mathbf{H}_{\mathbf{x}}^{i,o}$, and $\mathbf{n}_{\text{OF}}$ is a block vector with elements $\mathbf{n}_i^o$. We can use Eq. 22 to perform an EKF update with valid OFs. We call this step an MSCKF-based update.

We perform EKF updates when a processed ML/OF feature track becomes available or if the oldest IMU pose before marginalization has valid ML observations (cf. Algorithm 1). Upon the arrival of a new image, we find out all blob tracks that are newly lost. If MLs exist therein, we carry out a map-based update according to Eq. 20 using all the associated MLs. Rather than performing single updates with any individual ML in each frame as in [38], we use all the involved ML measurements that are part of a feature track to form a single constraint, inspired by [11]. After that, OFs tracked across multiple frames are used for an MSCKF-based update according to Eq. 22. The past poses in the sliding window can first get absolute corrections by MLs before we use them to triangulate feature positions for OFs. This helps improve the triangulation accuracy and hence benefit the MSCKF-based updates. The strategy works reasonably well in practice. When the sliding window is full, the oldest IMU pose gets marginalized out of the filter to keep bounded computation. If the pose relates to valid ML observations, we use them to perform a map-based update before marginalization while discarding any associated OFs. The above EKF updates can be carried out using general EKF equations [62].

VI. Experimental Evaluation

We conduct real-world experiments to study the system's performance in VLC decoding, localization, and odometry. We first introduce the experiment setup for hardware preparation and data collection in Section VI-A. We show the effectiveness of VLC decoding assisted with blob tracking in Section VI-B. Comparing with an EKF-based VLP baseline, we evaluate the localization performance on different motion profiles under various lighting conditions in Section VI-C. Moreover, we challenge our system in adverse scenarios with severe ML outages, and explicitly study the influence of OFs in Section VI-D. Next, we show the performance of running odometry with only OFs in Section VI-E. Finally, we evaluate the algorithm efficiency with runtime analysis in Section VI-F.

A. Experiment Setup

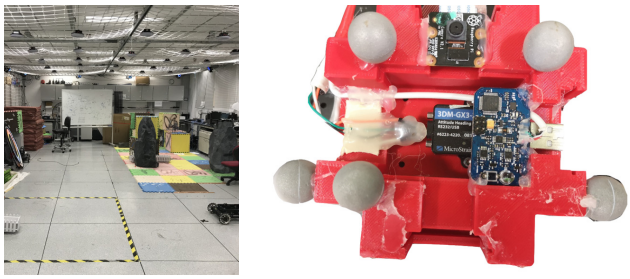

(a) Test field (b) Visual-inertial sensor suite

Fig. 4: Photos of the environment and self-assembled sensors.

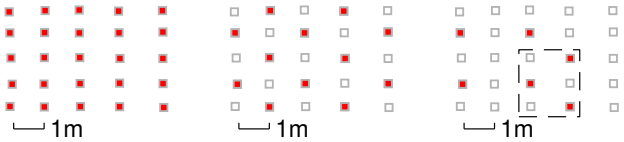

(a) **M25** (b) **M12** (c) **M06**

Fig. 5: Visualization of three LED maps for our tests. The modulated LEDs chosen as MLs are marked in red. The rest are treated as unmodulated lights to provide OFs and are marked in white.

We build 25 modulated LEDs powered by batteries and set up a room-sized test field ($5\,\text{m} \times 4\,\text{m} \times 2.3\,\text{m}$) with them evenly spaced on the ceiling, as shown in Fig. 4a. Each LED has a circular radiation surface of $15.5\,\text{cm}$ in diameter and rating power of $3\,\text{W}$[5]. A microcontroller runs the VLC protocol on its firmware and modulates the LED current via a metal-oxide-semiconductor field-effect transistor (MOSFET). The OOK modulation frequency is $16\,\text{kHz}$.

The visual-inertial sensor assembly comprises a MicroStrain 3DM-GX3-25 IMU and a Raspberry Pi 3B single-board computer with a Sony IMX219 rolling-shutter camera, as shown in Fig. 4b. There is no hardware synchronization between the camera and IMU sensors. We calibrate the camera intrinsics and the IMU-camera spatiotemporal extrinsics using Kalibr [64]. We feed these rough parameters into our estimator for online refinement. We minimize the camera's exposure time to capture clear strips from modulated LEDs. The camera's frame readout time t_r should be available in its manufacturing specifications. Otherwise, an initial guess of it suffices as it can be online refined by the estimator. To achieve this,

[5]This is characteristic of the raw LED light we bought on the market. In this work, we did not make any special choice on the emitting power.

we first compute the row readout time τ_r using the formula $\tau_r = \tau_m / \mathrm{w}_0$, where w_0 represents the minimum strip width in the strip pattern and τ_m is the LED's modulation period [58]. The frame readout time is given by $t_r = N\tau_r$ with N as the image height in pixels. τ_m and N are both known.

For existing evaluations, we assume that w_0 is roughly calibrated by hand before the operation. However, for real applications, w_0 can be inferred automatically by the software. The rationale is as follows. The VLC data packet begins with a 4-bit preamble symbol $\mathrm{PS} = \mathrm{b0001}$ and ends with another 4-bit symbol $\mathrm{ES} = \mathrm{b0111}$ (cf. the supplementary material [58]). The preamble produces a LOW-logic of the maximum width in the binary VLC signal (see Fig. 3), i.e., $3\mathrm{w}_0$. We first locate it by finding the widest LOW-logic and measure the symbol width in pixels (denoted as l) in a programmed manner. Then we have $\mathrm{w}_0 = l/3$ and $t_r = 3N\tau_m/l$. We use the obtained t_r as an initial guess and feed it into the estimator for refinement. This way, we can automate the calibration of t_r without assuming any known specifications or manual input.

The Raspberry Pi 3B (ARM Cortex-A53 CPU@1.2 GHz, 1 GB RAM) runs the sensor drivers on Ubuntu Mate 16.04 with robot operating system (ROS). The sensor data are streamed to it and stored as ROS bags. Unless otherwise specified, the data are ported to a desktop computer (Intel i7-7700K CPU@4.2 GHz, 16 GB RAM) for subsequent evaluation. The image data are collected at 10 Hz with a resolution of 1640×1232, and the IMU data are available at 200 Hz.

An OptiTrack[6] motion capture system (Mocap) provides 6-DoF ground truth poses at 120 Hz. The world frame for the Mocap system is set up to coincide with the global frame $\{G\}$. The 3D coordinates of LEDs in $\{G\}$ are obtained by a manual site survey with the help of Mocap and a commodity laser ranger. We collect 14 datasets in the test field using the handheld sensor suite with different walking profiles. The main characteristics are summarized in Table II. During the collection, we point the camera upwards to the ceiling. To ease filter initialization, we put the sensor on the ground at the start of each trial and leave it still for a few seconds.

TABLE II: Characteristics of 14 self-collected datasets.

No.	Duration [s]	Distance [m]	Max. Vel [m/s]	Name
1	48.69	40.64	1.32	circle-01
2	38.59	30.06	1.31	circle-02
3	33.99	27.88	1.35	circle-03
4	66.19	67.37	1.39	eight-01
5	45.89	43.59	1.48	eight-02
6	42.79	41.75	1.48	eight-03
7	36.80	52.41	2.59	fast-circle-01
8	32.60	36.78	1.97	fast-circle-02
9	66.99	69.05	1.47	random-01
10	46.49	45.94	1.52	random-02
11	132.68	158.83	1.65	random-03
12	39.89	34.71	1.46	square-01
13	33.89	27.53	1.31	square-02
14	40.99	43.00	1.45	square-03

Note that all lights employed here are physically modulated LEDs, and are registered in a prior map. They are primarily designed for MLs. For evaluation convenience, however, some can be intentionally unregistered, acting as regular unmodulated lights. With any prior knowledge discarded, these LEDs seamlessly provide only OFs. This gives us the flexibility to emulate different combinations of modulated LEDs and unmodulated lights in the test field. As illustrated in Fig. 5, we introduce three primary LED maps at different ML-sparsity levels: dense, medium and sparse, that respectively have 25, 12, and 6 LEDs registered as MLs, namely **M25**, **M12**, and **M06**. In each map, the unregistered LEDs act as unmodulated lights to provide OFs. The three MLs within the dotted square of Fig. 5c are specially used for the evaluation in Section VI-D.

[6]https://optitrack.com

B. VLC Decoding with Blob Tracking

We first test the VLC decoding performance achievable by our hardware setup when the camera is static. For a modulated LED, we define the decoding success rate as the ratio of the number of images with correct decoding results to the total number of images processed in a given time period. Table III shows the statistics on success rates for a single LED at varying LED-camera distances. The maximum decoding range achieved by our system is slightly over 2.5 m.

TABLE III: VLC decoding performance with a static camera.

LED-camera distance [m]	1.0	1.5	2.0	2.5	3.0
Decoding success rate [%]	98.2	88.3	72.2	16.8	0.0

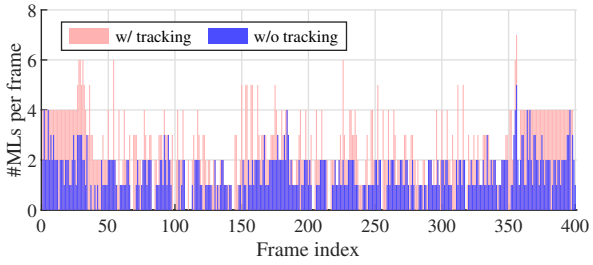

Fig. 6: Evolution of the number of detected MLs over frames, with and without blob tracking, on dataset *square-01* using map **M25**.

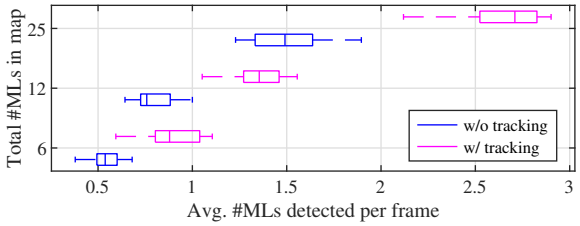

Fig. 7: Boxplot of the average number of MLs detected per frame across the 14 datasets, with and without blob tracking, using three maps with a different number of MLs, i.e., **M06**, **M12**, and **M25**.

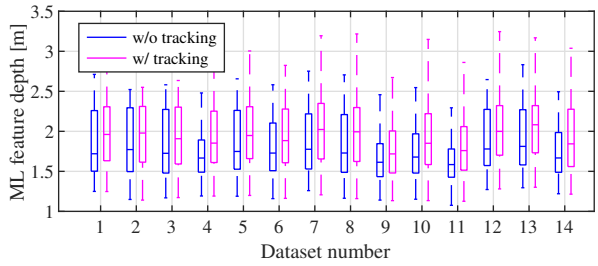

Fig. 8: Boxplot of feature depths for all the detected MLs on each of the 14 datasets using map **M25**, with and without blob tracking.

We then consider performing VLC decoding with a moving camera as this is more general in localization scenarios. Fig. 6 shows the time-evolving number of MLs detected per frame on dataset *square-01* using map **M25**, with and without blob tracking. Clearly, using blob tracking in our VLC frontend has efficiently increased the observation number of MLs on many frames. The boxplots in Fig. 7 summarize the average number of MLs detected per frame on all the 14 collected datasets, under different map configurations of **M06**, **M12**, and **M25**. Comparing the results in the tracking and non-tracking cases, we confirm the finding that, with blob tracking enabled, the frontend can produce more valid observations of MLs per frame for later localization. In this sense, blob tracking can improve the decoding performance during camera motion for the adopted rolling-shutter VLC mechanism.

To give some insights into how tracking helps in decoding, we individually present in Fig. 8 the feature depths of detected MLs on the 14 datasets. The feature depths are computed in the pose estimation procedure using map **M25**. In particular, the results in the tracking case are obtained by the proposed method, while those for the non-tracking case are obtained by our previous EKF-based solution [38]. We can observe that the feature depths of detected MLs are way greater in the tracking case. This is because blob tracking provides short-term data associations for tracked lights. The modulated LEDs that appear at faraway locations may not be decoded in time; yet, they still have a chance to be identified later as the camera moves closer. The median length of feature tracks obtained on the 14 datasets ranges from 8 to 13.

C. Localization using MLs and OFs

To our knowledge, there are no open-source implementations of inertial-aided VLP systems using modulated LEDs or unmodulated lights. In what follows, we treat our previous work [38] as a baseline for benchmark comparison. To be specific, we evaluate the proposed VLP system on 14 self-collected datasets (see Table II) using three LED feature maps of different ML-sparsity levels (see Fig. 5), i.e., **M06**, **M12**, and **M25**. By design, blob tracking in the frontend can benefit localization in two ways: 1) producing more observations of MLs for map-based updates, and 2) enabling the optional use of OFs for MSCKF-based updates. To study each of their contributions, we evaluate two variants of our proposed method. The first, named *SCKF* (stochastic cloning Kalman filter), performs map-based updates with detected MLs only. The second, named *MSCKF*, performs both map-based and MSCKF-based updates with all valid observations of MLs and OFs. We compare these two variants against [38], denoted as *EKF*, that tightly fuses inertial and ML measurements by a regular EKF without blob tracking in its VLC frontend.

The SCKF and MSCKF maintain $m = 11$ pose clones in the sliding window. To initialize the global pose for all three methods, we adopt a 2-point pose initialization method as in [38]. All the filter parameters are kept constant when running different methods on different trials. In particular, the process noise and measurement noise parameters are summarized in Table IV. We use the absolute trajectory error (ATE) [65] to measure global position accuracy and the axis-angle error to measure orientation accuracy. Online demonstrations are available in the supplementary video[7].

TABLE IV: Process noise and measurement noise parameters in use.

Param	σ_g	σ_{wg}	σ_a	σ_{wa}	σ_{im}	σ_f
Value	0.005	0.0001	0.05	0.002	0.03	0.03
Unit	$\frac{rad}{s\sqrt{Hz}}$	$\frac{rad}{s^2\sqrt{Hz}}$	$\frac{m}{s^2\sqrt{Hz}}$	$\frac{m}{s^3\sqrt{Hz}}$	unitless	m

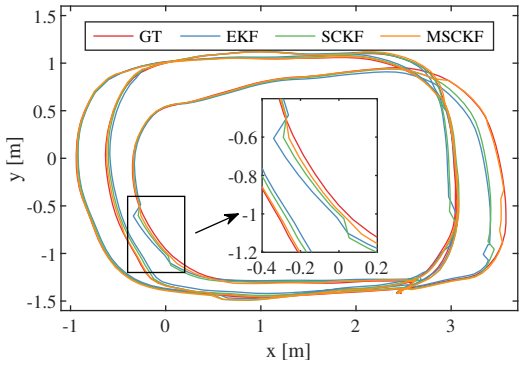

Fig. 9: Top-view of the trajectories estimated by different methods, as well as the ground truth, on dataset *square-01* using map **M06**.

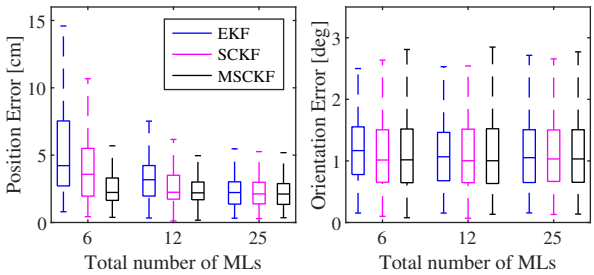

Fig. 10: Error statistics by different methods on dataset *square-01* using three maps with different numbers of MLs.

In Table V, we report the root mean squared error (RMSE) for the global position and orientation estimates on 14 datasets with different combinations of maps and methods. We provide more detailed results on sequence *square-01*. It travels $35\,\text{m}$ in $40\,\text{s}$ along squares at a maximum speed of $1.46\,\text{m/s}$. The boxplots in Fig. 10 summarize the statistics of the absolute position and orientation errors. In particular, Fig. 9 shows the estimated trajectories using the sparsest map **M06**. The results by three methods can fit the ground truth at most locations, and MSCKF exhibits fewer mismatches than others, as shown in the zoomed area and on the rightmost side of Fig. 9.

Position results: We can see from Fig. 10 that for each of the EKF, SCKF, and MSCKF methods, the position errors tend to decrease with more MLs in the map. The finding can be well supported by Table V as we compare the columns of the position RMSE results that correspond to different maps. For all methods, MLs provide absolute geometric constraints that render the global position observable. With sparser MLs, the global position accuracy becomes more vulnerable due to insufficient constraints of such kind.

In the case of sparse MLs (e.g., **M06** and **M12**), our MSCKF and SCKF methods generally outperform the EKF baseline in

[7]https://youtu.be/I7h1Ojv1-f8

TABLE V: Error statistics on 14 datasets using maps of **M06**, **M12**, and **M25**. Bold font highlights the best result in each row.

M06	Position RMSE [cm]			Orientation RMSE [deg]		
No.	EKF	SCKF	MSCKF	EKF	SCKF	MSCKF
1	2.78	2.75	**2.72**	**1.14**	1.23	1.24
2	5.11	5.46	**3.33**	1.33	**1.32**	1.34
3	4.71	3.34	**3.18**	**1.30**	1.33	1.39
4	5.35	4.91	**4.07**	2.06	**2.05**	2.06
5	5.15	4.35	**4.24**	1.54	**1.49**	1.51
6	4.82	4.09	**3.33**	1.65	**1.60**	1.63
7	8.11	6.98	**4.73**	**1.96**	2.05	2.12
8	8.10	6.50	**4.62**	**1.39**	1.47	1.51
9	7.02	7.50	**4.34**	1.57	1.57	**1.56**
10	15.23	13.38	**6.13**	**1.83**	1.89	1.90
11	12.82	9.41	**4.66**	**1.61**	**1.61**	1.62
12	8.40	5.77	**2.92**	1.33	**1.27**	1.28
13	5.40	4.17	**2.76**	**1.23**	1.34	1.30
14	6.25	4.26	**3.65**	1.84	**1.75**	**1.75**
M12	Position RMSE [cm]			Orientation RMSE [deg]		
No.	EKF	SCKF	MSCKF	EKF	SCKF	MSCKF
1	**2.38**	2.44	2.46	**1.16**	1.23	1.24
2	2.70	2.63	**2.54**	1.32	**1.31**	1.33
3	4.19	3.04	**2.86**	**1.33**	1.40	1.41
4	4.04	3.91	**3.01**	2.01	2.04	**1.60**
5	4.08	**3.88**	3.97	**1.51**	**1.51**	**1.51**
6	3.90	3.37	**3.21**	**1.58**	1.61	1.63
7	3.54	3.25	**3.12**	**2.02**	2.11	2.11
8	4.20	3.40	**3.10**	**1.49**	1.58	1.56
9	3.34	3.27	**3.19**	**1.56**	**1.56**	1.57
10	4.96	3.57	**3.00**	**1.80**	1.82	1.84
11	3.96	3.68	**3.48**	**1.60**	1.62	1.63
12	4.15	3.19	**2.70**	**1.27**	**1.27**	1.28
13	4.37	3.67	**2.67**	**1.24**	1.37	1.33
14	4.89	3.23	**3.08**	1.85	**1.80**	**1.80**
M25	Position RMSE [cm]			Orientation RMSE [deg]		
No.	EKF	SCKF	MSCKF	EKF	SCKF	MSCKF
1	**2.02**	2.17	2.18	**1.18**	1.20	1.21
2	**1.99**	2.29	2.28	1.32	**1.28**	1.29
3	2.29	2.17	**2.13**	**1.30**	1.35	1.35
4	**3.24**	3.30	3.31	**2.01**	2.02	2.02
5	2.78	2.52	**2.50**	1.51	1.47	**1.46**
6	**2.33**	2.43	2.42	**1.53**	**1.53**	**1.53**
7	**2.51**	2.59	2.54	2.06	2.05	**2.01**
8	2.47	2.39	**2.36**	1.62	**1.60**	**1.60**
9	2.57	**2.56**	2.57	**1.54**	1.55	1.55
10	2.73	**2.54**	**2.54**	**1.77**	1.78	1.78
11	**3.24**	3.39	3.33	1.59	**1.58**	**1.58**
12	2.82	2.56	**2.52**	**1.28**	**1.28**	**1.28**
13	2.73	2.38	**2.36**	**1.33**	1.35	1.34
14	2.54	**2.45**	2.47	1.82	**1.66**	**1.66**

terms of position accuracy, and the MSCKF often performs the best. This is evident in the corresponding boxplots in Fig. 10 and is validated by most cases in the corresponding rows of Table V. The performance gain of our MSCKF and SCKF methods against the EKF is due in part to their inclusion of more ML observations, produced by the visual frontend with blob tracking, for map-based updates. Compared with the SCKF, the MSCKF makes extra use of OFs observed from unmodulated lights or undecoded LEDs to provide relative motion constraints. This helps to reduce its pose drift during ML outages and improve localization accuracy. On this point, we provide more detailed evaluations later in Section VI-D.

With dense ML deployments (e.g., **M25**), however, all three methods deliver closely high position accuracies, as shown by Fig. 10 and the bottom rows of Table V. In this case, we suspect the number of MLs detected per frame is no longer the performance bottleneck as previously. All methods can be sufficiently constrained because of rich ML occurrences. The advantage of blob tracking for the MSCKF and SCKF is now not as pronounced as in the sparse-ML case. Furthermore, the performance difference between these two variants is marginal. This is because all 25 LEDs have been registered as MLs, and only those that fail in VLC decoding occasionally serve OFs. The limited use of OFs renders the MSCKF almost degenerated to the SCKF variant. Interestingly, the EKF has achieved slightly smaller position RMS errors than ours on a few datasets (see #1, #2, etc.). This is likely due in part to the method of using MLs for updates. Upon the arrival of an image input, the EKF can perform a map-based update soon with the newly detected MLs. By contrast, the sliding window mechanism in the MSCKF and SCKF introduces an additional latency for each tracked ML before its use. Note that MLs in our methods are processed when they lose tracking or the oldest pose is marginalized out. The delayed update may have side effects on real-time localization in the sense that absolute pose corrections are not applied so timely as in the EKF.

To conclude, in terms of absolute position performance, our MSCKF method has consistently achieved high accuracies of centimeter-level RMSE on all 14 datasets using three LED maps. It shows better robustness than others to the sparsity of MLs within the map. We credit these advantages to making full use of more MLs and optional OFs for localization, which are more pronounced in scenarios with sparse MLs.

Orientation results: From Fig. 10 and Table V, we can see that the absolute orientation errors by all three methods are very close to each other using maps of different ML-sparsities. The orientation RMS errors on all test cases are around 1-2 degrees. The advantage of the MSCKF method in orientation estimation becomes less obvious than in position estimation. We attribute this mainly to the fact that tracking orientation accurately is much easier than tracking position using an IMU.

We see that all methods tightly fuse inertial and visual measurements by Kalman filtering for pose estimation. The pose is tracked with IMU double-integration and is corrected intermittently by ML/OF measurements. The global roll and pitch are observable owing to known gravity constraints. Their estimates are drift-free. Yet, the global yaw and position are observable in the presence of MLs, i.e., known 3D features that provide absolute geometric constraints. During the outage of MLs, the related estimates will drift but to different degrees.

The drift arises from the accumulated errors by IMU double-integration, in which position errors grow much faster than orientation errors. Let us consider a period between two EKF updates. The global yaw can suffer from linear errors with time due to uncorrected gyroscope biases. By contrast, the global position can suffer from quadratic or even cubic errors with time due to uncorrected IMU biases. Within a short integration time (e.g., a few seconds), the induced yaw drift is much smaller and easier to correct using intermittent MLs. This way, orientation errors in three directions can be all bounded small.

To summarize, with intermittent ML corrections, the three methods can achieve closely high performance in orientation estimation owing to the known gravity constraint and the inherent characteristic of slowly-growing yaw errors in ML outages. By contrast, achieving accurate position estimates in the long term is more difficult due to the fast-growing position errors in IMU double-integration and the lack of observability in 3D position during ML outages. This is a major challenge we aim to address. As shown earlier, our MSCKF method can

effectively reduce this position drift by midway corrections using OFs, thus improving the overall positional performance.

D. Localization under Challenging Conditions

We challenge our system under unfavorable conditions, such as severe outages of MLs and the shortage of OFs due to the highly sparse placement of modulated LEDs/unmodulated lights. Through the experiments, we aim to study 1) the influence of the sparsity of OFs on localization accuracy and 2) the importance of OFs to the system operation. For evaluation, we use a very sparse map, **M03**, with three out of 25 LEDs as MLs, as highlighted by the dotted square in Fig. 5c. The start and end points for data collection are within this area. This enables the estimator to initialize its global pose by the 2-point pose initialization [38] at startup. Using three and not two MLs allows better initial pose guesses from more constraints. We treat the other 22 LEDs as *unmodulated lights*.

The setup of 22 unmodulated lights in a $5\,\mathrm{m} \times 4\,\mathrm{m}$ sized area represents a dense deployment, comparable to the original setup of 20 fluorescent tubes. Changing the deployment of unmodulated lights allows us to test the system with OFs of different sparsities. For evaluation convenience, we do not alter the physical setup of the lights. Alternatively, we emulate a few different sparse-deployment cases by dropping out a part of the OF tracks produced by the frontend. This is achieved by removing unwanted OFs as per the feature ID. We can flexibly control the number of OFs in use by choosing a different usage rate. In the experiments, we keep $\{100, 50, 25, 10, 0\}$ percent of the originally detected OFs. In the case of 0% OFs, the MSCKF method degenerates to SCKF since no OFs are used for updates. The other experiment settings remain unchanged. We run MSCKF on the 14 datasets using map **M03** and with OF usage rates of $\{100, 50, 25, 10, 0\}$ percent.

Influence of OF sparsity on localization accuracy: As shown in Fig. 11, we present the detailed results on dataset *square-01*. Fig. 11a shows the evolution of absolute position errors over time. With three MLs, the system has experienced the frequent absence of ML observations. This is also referred to as ML outages (see the shaded area in Fig. 11a). We observe that the position errors are well constrained in the presence of MLs, regardless of how many OFs are involved. During ML outages, however, the position errors grow more evidently when fewer OFs are used. Given 0% OFs, the method fails on this dataset. We believe that OFs are more important to the system in the situation of ML outages. Fig. 11c shows the boxplots of the absolute position and orientation errors. The position errors grow as the OF usage rate decreases, whereas the orientation errors do not change significantly. Fig. 11b shows how the exact number of OFs evolves per frame as the OF usage rate varies at $\{100, 50, 25, 10\}$ percent. The number of OFs averaged over all frames is $\{3.65, 1.84, 0.98, 0.41\}$, respectively. The MSCKF can run successfully on dataset *square-01* with 0.41 OFs or more per frame on average. Given fewer OFs, it is prone to a complete failure. It seems that the more OFs that are used, the better the position accuracy.

The results on the 14 datasets are reported in Table VI. We characterize the richness of OF observations by the average

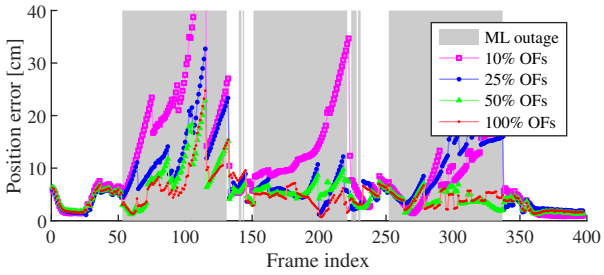

(a) Evolution of position errors over consecutive frames.

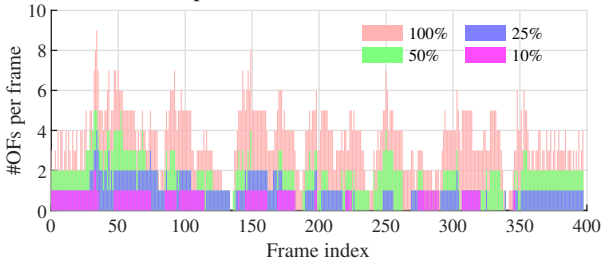

(b) Evolution of the number of OFs in use per frame.

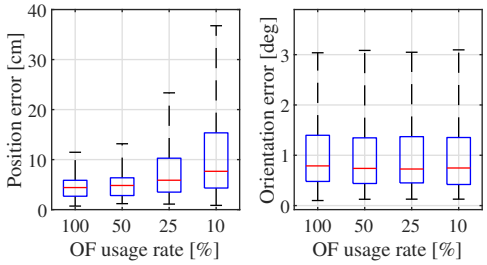

(c) Statistics of the absolute position and orientation errors.

Fig. 11: Results of the MSCKF method on dataset *square-01* using map **M03** and with OF usage rates of $\{100, 50, 25, 10\}$ percent.

number of OFs over all frames. The absolute pose errors are quantified by the position and orientation RMSE. In the last row, we loosely summarize the results across all datasets by averaging valid entries to provide an overall scalar metric. As shown by the leftmost 100% column, the average number of OFs per frame varies among datasets, ranging from 2.66 to 3.71. With OF usage rates of $\{100, 50, 25, 10, 0\}$ percent, the average number of OFs per frame over all datasets is $\{3.27, 1.62, 0.82, 0.36, 0\}$. Without OFs, our method fails on 8 out of 14 datasets (see 0% columns). With 10% OFs (i.e., 0.36 per frame), it succeeds on all but one dataset (#11). Further, with 25% OFs (i.e., 0.82 per frame) or more, the method runs successfully on all test cases. We can see from these successful runs in Table VI that, in our experiments with very sparse MLs, the position errors generally increase with fewer OFs. Nevertheless, we have reached a 3D position accuracy of decimeters. This is close to if not better than the best performance of many existing radio localization methods like WiFi fingerprinting [66], [67]. When the OF usage rate changes, the orientation errors do not differ significantly in most cases. The reason for this is explained in Section VI-C.

To summarize, the results have reinforced our claim that OFs help improve the position accuracy by reducing pose drift during the ML outage. Especially, given sparse MLs, the

TABLE VI: Results of the MSCKF method on the 14 datasets using map **M03** and with OF usage rates of $\{100, 50, 25, 10, 0\}$ percent. The $\times$ sign indicates running failures. The last row shows the average quantity over all valid entries in each column.

No.	#OFs averaged over frames					Position RMSE [cm]					Orientation RMSE [deg]				
	100%	50%	25%	10%	0%	100%	50%	25%	10%	0%	100%	50%	25%	10%	0%
1	3.54	1.78	0.86	0.58	0	4.87	6.27	6.76	7.71	22.64	0.95	0.99	0.99	1.00	1.08
2	2.83	1.56	0.68	0.34	0	5.01	9.07	13.49	21.98	×	1.01	1.01	1.02	1.03	×
3	3.01	1.54	0.79	0.51	0	4.60	4.92	5.31	6.77	9.17	1.20	1.20	1.21	1.21	1.20
4	3.68	1.89	0.99	0.42	0	4.83	6.23	6.93	16.25	×	1.14	1.22	1.23	1.39	×
5	3.71	1.96	0.87	0.38	0	4.36	5.66	6.43	14.04	15.02	1.02	1.05	1.08	1.14	1.25
6	3.36	1.60	0.85	0.27	0	4.34	4.88	6.50	12.69	13.31	0.96	0.94	0.96	0.97	1.00
7	3.21	1.51	0.70	0.47	0	8.91	9.52	10.56	26.16	×	2.27	2.27	2.14	2.25	×
8	3.35	1.50	0.83	0.22	0	6.13	9.30	10.72	12.62	42.60	1.21	1.21	1.16	1.17	1.57
9	2.89	1.45	0.73	0.28	0	7.33	10.20	11.71	25.39	×	1.03	1.03	1.06	1.07	×
10	3.33	1.69	0.93	0.31	0	8.93	9.47	9.93	19.68	×	1.35	1.31	1.28	1.32	×
11	3.12	1.56	0.81	0.31	0	8.42	11.36	27.57	×	×	1.11	1.18	3.30	×	×
12	3.65	1.84	0.98	0.41	0	5.84	6.24	9.50	14.74	×	1.19	1.16	1.17	1.16	×
13	3.44	1.58	0.86	0.35	0	3.81	5.46	7.54	19.39	29.45	1.03	1.10	1.09	1.18	1.32
14	2.66	1.27	0.60	0.19	0	8.35	12.6	20.70	74.13	×	1.25	1.30	1.36	1.31	×
Avg.	3.27	1.62	0.82	0.36	0	6.12	7.94	10.98	20.89	22.03	1.19	1.21	1.36	1.25	1.24

TABLE VII: Statistics of two metrics characterizing ML outages on the 14 datasets: the outage rate and the maximum outage duration.

Dataset	No.	1	2	3	4	5	6	7	8	9	10	11	12	13	14
	Label	c1	c2	c3	e1	e2	e3	f1	f2	r1	r2	r3	s1	s2	s3
ML outage	Rate [%]	45	49	45	61	58	54	63	62	69	59	77	61	50	70
	Max. [s]	5.2	6.8	4.4	4.8	4.6	4.0	4.8	5.3	12.2	6.5	12.6	8.5	5.1	9.6

position performance improves with more OFs. Be noted that the maximum number of OFs per frame is bounded in reality, e.g., by the density of lights, ceiling height, and camera FoV.

Importance of OFs to system operation: Then we ask the question, "*At least how many OFs per frame should there be to run the system successfully?*" We see from Table VI that the minimum number of OFs for success varies among datasets. For instance, the system has succeeded on 6 out of 14 datasets (e.g., #1, #3, etc.) without using OFs. Running on dataset #11, it needs 25% OFs or more to work. As discussed earlier, we believe that OFs are more critical to the system given ML outages and otherwise not (see Fig. 11a). The outage is partly due to the highly sparse deployment of MLs, e.g., using three MLs in this evaluation. In addition, due to various motion patterns, individual datasets could experience ML outages to different degrees. To quantify the outage level, we propose the below two metrics:

- ML outage rate. This is the ratio of accumulated time of ML outages to the total time. This rate indicates how often the outage happens and to which degree as a whole.
- Max. outage duration. This captures the most challenging outage situation. Note that the system could fail with severe pose drift due to a single long-term outage.

We use these together to characterize the outage situation. The statistics of these metrics on 14 datasets are summarized in Table VII and are visualized by the scatterplot in Fig. 12. The labels in Fig. 12 indicate the datasets in a way described by Table VII. The ML-outage rate is 45% or higher, with the maximum 77% achieved on dataset #11. The maximum ML-outage duration is between $4.0\,\mathrm{s}$ and $12.6\,\mathrm{s}$. In Fig. 12, the datasets on the upper right suffer from more ML outages than those on the lower left. The system can run successfully with no OFs on datasets indicated by squares. Running on datasets indicated by crosses, it needs 10% OFs (i.e., 0.36 per frame) or more. When running on the most challenging dataset #11, it needs 25% OFs (i.e., 0.82 per frame) or more. According to these findings, the minimum number of OFs per frame for system operation closely depends on the ML-outage level. The more ML outages, the more OFs are needed for success.

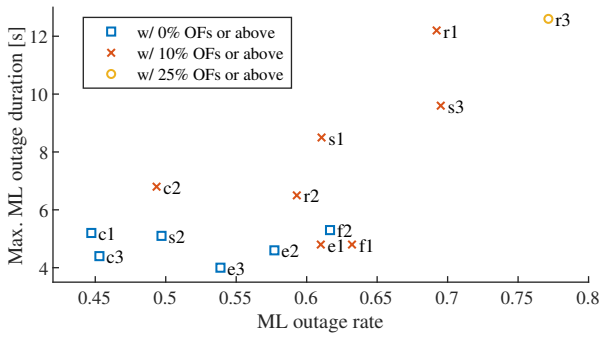

Fig. 12: Scatterplot showing the distribution of 14 datasets along two dimensions of the outage rate and maximum outage duration. Markers indicate a different number of OFs needed for success.

E. Odometry Performance using OFs only

Previously, MLs are essential to the system for localization, while OFs can be optional. In this section, we aim to explore the odometry performance of the VLP system using OFs only. Here, we treat all the 25 LEDs as unmodulated lights such that they serve as OFs. Without MLs for map-based updates, the system degenerates to a variant of the regular MSCKF VIO [2]. Instead of using natural point features, it works with blob features (i.e., OFs) from ceiling lights. We initialize the filter at rest. Unlike in the previous settings, we tune the initial covariances of the position and orientation in the filter to accommodate the small initial uncertainty for a VIO setup. Other parameters remain unchanged. We aim to see if the system can run VIO based on OFs, and to achieve this, how many OFs there should be at least. We control the number of OFs per frame for evaluation as in Section VI-D.

Position results: We run the system in VIO mode on 14 datasets with different OF usage rates of $\{100, 50, 25, 10\}$

percent. Fig. 13 shows the boxplots of the average number of OFs per frame and the position RMSE on all datasets. The position errors are computed after trajectory alignment using the *posyaw* method in [68]. When the OF usage rate changes among $\{100, 50, 25, 10\}$ percent, the average number of OFs per frame on all datasets is $\{3.59, 1.78, 0.90, 0.36\}$. OFs from unmodulated lights are considerably sparser than natural point features[8]. The system can run VIO successfully on all datasets while using 25% OFs or more. But given 10% OFs, it fails to run the complete sequence on 9 out of 14 datasets. With 25% OFs, the average number of OFs per frame is 0.90. So we roughly say that the system can run VIO based on OFs when supplied with around one or more OFs per frame. The position RMSE averaged on successful runs is $\{0.22, 0.26, 0.34, 0.51\}$ meter. The position accuracy degrades with fewer OFs, largely due to insufficient visual constraints.

The system has a high tolerance to the sparsity of OFs when running odometry. We try to explain it from two aspects. First, light blobs are good features to detect and track. Given sparse blob features, the visual frontend can track them without using random sample consensus (RANSAC) for outlier rejection. Yet, this may not apply to natural features in standard VIO. Second, the system can resolve poses recursively in a tightly coupled way such that any individual feature measurement, however sparse, can be adopted. On the downside, this sparsity can also cause insufficient geometric constraints and compromises the tracking performance, as shown below.

***Tracking results**:* We assess the tracking performance in terms of relative pose errors [68], [69]. We run the system in VIO mode on dataset #11 (*random-03*) with a different OF usage rate of $\{100, 50, 25\}$ percent and present the results in Fig. 14. Note that it fails to run with 10% OFs. Dataset #11 is the longest among all datasets, traveling around $160\,\mathrm{m}$ in $133\,\mathrm{s}$. Also included for comparison are the results of the proposed MSCKF method using map **M03**.

Fig. 14a shows the estimated trajectories after alignment using the *posyaw* method in [68] alongside the ground truth. Fig. 14b shows the relative translation and yaw errors. As seen from Fig. 14, the VIO trajectories estimated using fewer OFs are more jittery and drift-prone; and the related translation and yaw errors grow with the traveled distance, as expected. The mean translation drift error computed by [68] is 1.12%, 1.39%, and 1.63%, for the OF usage rate of $\{100, 50, 25\}$ percent, respectively. The odometry estimates suffer when fewer OFs are used, due to insufficient constraints from OFs. Meanwhile, with the aid of 3 MLs only, the relative pose errors become much smaller; and the mean translation drift is reduced to 0.29%. Here, the relative pose errors do not grow with the traveled distance due to the global localization nature.

To summarize, our system can run VIO standalone with very sparse OFs. This supports our original idea of using OFs to reduce pose drift during ML outages. Especially in the case of long-term outages, even sparse OFs help to sustain the overall system. However, the odometry performance is very likely inferior to regular VIO due to feature sparsity. Therefore, rather than running VIO based on OFs, we would like to use them as a beneficial supplement to MLs for global localization.

[8]The maximum number of OFs detected per frame is no more than a dozen in our tests due to the sparsity of lights. By contrast, standard VIO systems often work with a few tens or hundreds of point features per frame.

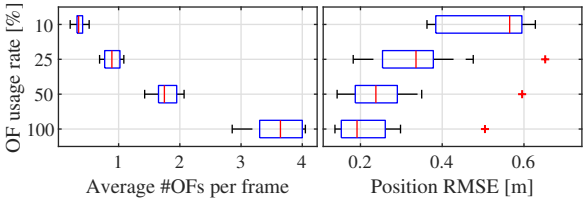

Fig. 13: Results on 14 datasets when the system runs VIO with different OF usage rates. Failures occur with 10% OFs in use.

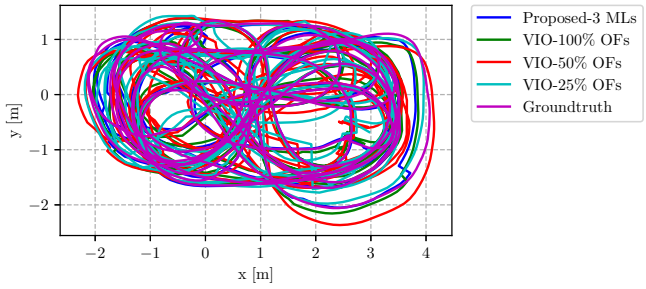

(a) Top-view of the estimated trajectories and ground truth.

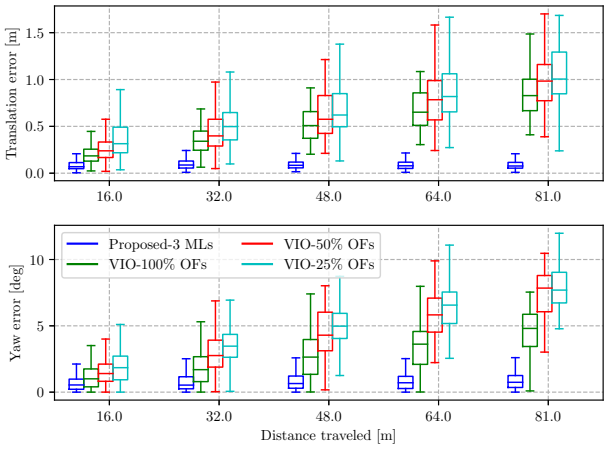

(b) Relative translation and yaw errors evaluated by [68].

Fig. 14: Results on dataset #11 when the system runs VIO with different OF usage rates. The localization results of our proposed MSCKF with 3 MLs are included for comparison.

F. Runtime Analysis

To evaluate processing efficiency, we run the proposed algorithms on a low-end Raspberry Pi 3B single-board computer. We implement two threads, i.e., the VLC frontend and the estimator. Table VIII summarizes the average time to process an image input by each thread on dataset *square-01*. We can see that the VLC thread dominates the runtime. The algorithm efficiency can be improved by optimizing the image processing pipeline. Due to the maintenance of a large state vector, the proposed system with a sliding window EKF formulation (i.e., SCKF, MSCKF) consumes more time than our previous EKF estimator. The blob tracking module also causes a slight increase in time (around $20\,\%$). Even so, we have achieved

real-time performance on Raspberry Pi 3B given a camera frame rate of 10 Hz. Our system remains lightweight to run on resource-constrained computational platforms.

TABLE VIII: Timing results of the VLC frontend and estimator of our proposed system running on a standard desktop PC and a Raspberry Pi 3B for a collected dataset, compared with those of [38].

Thread	VLC frontend [ms]		Estimator [ms]		
Platform	w/o track.	w/ track.	EKF	SCKF	MSCKF
Desktop PC	3.28	3.98	0.94	2.18	2.22
Raspi 3B	40.70	50.39	10.01	28.26	29.02

VII. Discussions

The proposed system has some limitations.

Firstly, we use circular LEDs of the same size and power for demonstration and evaluation. This is mainly due to our practical difficulty in preparing some homemade LEDs of different form factors. The blob detector and tracker in the frontend are currently designed for circular lights. However, the system would still work with other shaped lights if the proper blob detectors and trackers are designed for them. We will adapt the system to more types of lights in future work.

The system's communication and localization performance could be affected given the use of different-powered LEDs. The inbuilt automatic gain control (AGC) of image sensors allows the camera to adapt to certain levels of lighting changes. Hence, moderate changes in LED power are less likely to affect our performance. If the LED's intensity changes greatly from our existing settings, we can modify the blob detection process to accommodate this. Rather than binarizing the input image with a fixed threshold, we prefer adaptive thresholding like Otsu's method [70]. Still, the impact of LED power on system performance needs further investigation in future work.

Secondly, due to the limited LEDs at hand, the system was only tested in a room-sized environment. However, we argue that it is well scalable by design with the following justifications. 1) The modulated LEDs constitute a distributed VLC broadcasting network with one-way communication. According to [32], the VLC function naturally scales to the workspace scope and the concurrent number of VLC receivers (or users). 2) The system works with a highly sparse LED map. The required memory is almost negligible in comparison to conventional visual or LiDAR maps. Therefore, the workspace scope is unlikely to cause immediate limitations to our system.

However, the number of encodable LEDs can limit the scope in use. This number is determined by the channel capacity supported by the VLC network. Using modulated LEDs with a larger surface than our prototypes (which are very small-sized) or replacing our basic VLC implementation with one that is more advanced, the channel capacity can be safely increased.

Creating an accurate map of MLs efficiently is another problem critical to the large-scale deployment of our system in reality. Given an up-to-date architectural floor plan with detailed location annotations for lights, the map creation would be straightforward. However, this knowledge can be difficult to obtain in practice, e.g., due to privacy concerns. Manual site-survey using professional surveying instruments like a total station can be a valid option in practice; however, the incurred human labor and time could be costly. An automated LED mapping solution is more desired for real large-scale deployment. We leave this to our future work.

Finally, the system relies on ceiling lights and an upward-facing camera for normal operation. The orientation changes in roll and pitch are sometimes limited during motion. The system can accommodate large changes by inertial tracking at the risk of losing light observations. Improving the tracking performance with natural visual features is helpful, but is at the cost of adding a second camera with normal exposure.

VIII. Conclusion

In this paper, we proposed a novel inertial-aided VLP system using a rolling-shutter camera for lightweight indoor localization on resource-constrained platforms. Specially, we made full use of modulated LEDs and unmodulated lights as landmarks within a sliding-window filter-based sensor fusion framework, for the first time to our knowledge. We utilized a minimal sensor suite composed of a rolling-shutter camera and an unsynchronized IMU. The system comprised an image processing frontend and an EKF estimator. The frontend extracted two types of blob features (i.e., MLs, OFs) by blob detection, tracking, and optional VLC decoding. Essential to our system, the MLs provided absolute geometric constraints of known data associations to help correct accumulated drift and enable fast relocalization. Meanwhile, the OFs provided additional visual cues for relative pose estimation, which is helpful in reducing pose drift during ML outages. To handle delayed ML measurements and use OFs, we followed the stochastic cloning sliding window EKF framework of MSCKF and its multi-state constraint measurement model. The estimator tightly fused MLs, OFs, and inertial measurements for localization.

For system evaluation, we conducted extensive field tests in a room-sized environment equipped with 25 ceiling LEDs. The efficiency of the blob tracking-assisted VLC decoding strategy was demonstrated. Compared to our previous ML-only EKF solution, the system showed superior positional accuracy and robustness under challenging light configurations, owing to the full use of MLs and OFs. Evaluated on 14 self-collected datasets and using maps of 6, 12, and 25 MLs, the system consistently achieved global position accuracy of a few centimeters and orientation accuracy of up to one or two degrees. We explicitly showed that OFs facilitated improving position accuracy by reducing pose drift during ML outages. The importance of OFs to the system closely depended on the ML-outage situation experienced. Additionally, we explored the odometry performance of our system when supplied with OFs only. It managed to run VIO standalone with very sparse OFs (e.g., one OF per frame on average), despite its inferior tracking performance. Still, the finding encourages us that even sparsely distributed OFs can help sustain the system in the adverse case of long-term ML outages. With runtime analysis, finally, we demonstrated that the system is lightweight to run on resource-constrained platforms in real-time.

In future work, we plan to generalize the system to more types of lights, e.g., squared panels and linear tubes. For practical deployment of our system at scale, automated LED

mapping solutions are also of necessity. With a second camera that is normally exposed, we can further use natural features to facilitate pose tracking and improve the overall localization.

REFERENCES

[1] G. Huang, "Visual-inertial navigation: A concise review," in *Proc. IEEE Int. Conf. Robot. Autom. (ICRA)*. IEEE, 2019, pp. 9572–9582.

[2] A. I. Mourikis and S. I. Roumeliotis, "A multi-state constraint Kalman filter for vision-aided inertial navigation," in *Proc. IEEE Int. Conf. Robot. Autom. (ICRA)*. IEEE, 2007, pp. 3565–3572.

[3] M. Li and A. I. Mourikis, "Improving the accuracy of EKF-based visual-inertial odometry," in *Proc. IEEE Int. Conf. Robot. Autom. (ICRA)*. IEEE, 2012, pp. 828–835.

[4] ——, "Online temporal calibration for camera–IMU systems: Theory and algorithms," *Int. J. Rob. Res.*, vol. 33, no. 7, pp. 947–964, 2014.

[5] K. Sun, K. Mohta, B. Pfrommer, M. Watterson, S. Liu, Y. Mulgaonkar, C. J. Taylor, and V. Kumar, "Robust stereo visual inertial odometry for fast autonomous flight," *IEEE Rob. Autom. Lett.*, vol. 3, no. 2, pp. 965–972, 2018.

[6] Z. Yang and S. Shen, "Monocular visual–inertial state estimation with online initialization and camera–IMU extrinsic calibration," *IEEE Trans. Autom. Sci. Eng.*, vol. 14, no. 1, pp. 39–51, 2016.

[7] T. Qin, P. Li, and S. Shen, "VINS-Mono: A robust and versatile monocular visual-inertial state estimator," *IEEE Trans. Rob.*, vol. 34, no. 4, pp. 1004–1020, 2018.

[8] Apple, "Apple ARKit," https://developer.apple.com/augmented-reality/, accessed: 2020-05-12.

[9] Google, "Google ARCore," https://developers.google.com/ar/, accessed: 2020-05-12.

[10] T. Schneider, M. Dymczyk, M. Fehr, K. Egger, S. Lynen, I. Gilitschenski, and R. Siegwart, "Maplab: An open framework for research in visual-inertial mapping and localization," *IEEE Rob. Autom. Lett.*, vol. 3, no. 3, pp. 1418–1425, 2018.

[11] S. Lynen, T. Sattler, M. Bosse, J. A. Hesch, M. Pollefeys, and R. Siegwart, "Get out of my lab: Large-scale, real-time visual-inertial localization," in *Robotics: Science and Systems*, vol. 1, 2015.

[12] R. C. DuToit, J. A. Hesch, E. D. Nerurkar, and S. I. Roumeliotis, "Consistent map-based 3D localization on mobile devices," in *Proc. IEEE Int. Conf. Robot. Autom. (ICRA)*. IEEE, 2017, pp. 6253–6260.

[13] J. Surber, L. Teixeira, and M. Chli, "Robust visual-inertial localization with weak GPS priors for repetitive UAV flights," in *Proc. IEEE Int. Conf. Robot. Autom. (ICRA)*. IEEE, 2017, pp. 6300–6306.

[14] A. I. Mourikis, N. Trawny, S. I. Roumeliotis, A. E. Johnson, A. Ansar, and L. Matthies, "Vision-aided inertial navigation for spacecraft entry, descent, and landing," *IEEE Trans. Robot.*, vol. 25, no. 2, pp. 264–280, 2009.

[15] Y. Sun, M. Liu, and M. Q.-H. Meng, "Improving RGB-D SLAM in dynamic environments: A motion removal approach," *Rob. Auton. Syst.*, vol. 89, pp. 110–122, 2017.

[16] ——, "Motion removal for reliable RGB-D SLAM in dynamic environments," *Rob. Auton. Syst.*, vol. 108, pp. 115 – 128, 2018.

[17] J. Cheng, H. Zhang, and M. Q.-H. Meng, "Improving visual localization accuracy in dynamic environments based on dynamic region removal," *IEEE Trans. Autom. Sci. Eng.*, 2020.

[18] X. Zuo, P. Geneva, Y. Yang, W. Ye, Y. Liu, and G. Huang, "Visual-inertial localization with prior LiDAR map constraints," *IEEE Rob. Autom. Lett.*, vol. 4, no. 4, pp. 3394–3401, 2019.

[19] X. Ding, Y. Wang, D. Li, L. Tang, H. Yin, and R. Xiong, "Laser map aided visual inertial localization in changing environment," in *Proc. IEEE/RSJ Int. Conf. Intell. Robots Syst. (IROS)*. IEEE, 2018, pp. 4794–4801.

[20] S. Lynen, M. W. Achtelik, S. Weiss, M. Chli, and R. Siegwart, "A robust and modular multi-sensor fusion approach applied to MAV navigation," in *Proc. IEEE/RSJ Int. Conf. Intell. Robots Syst. (IROS)*. IEEE, 2013, pp. 3923–3929.

[21] S. Weiss, M. W. Achtelik, M. Chli, and R. Siegwart, "Versatile distributed pose estimation and sensor self-calibration for an autonomous MAV," in *Proc. IEEE Int. Conf. Robot. Autom. (ICRA)*. IEEE, 2012, pp. 31–38.

[22] G. Cioffi and D. Scaramuzza, "Tightly-coupled fusion of global positional measurements in optimization-based visual-inertial odometry," *arXiv preprint arXiv:2003.04159*, 2020.

[23] Y. Yu, W. Gao, C. Liu, S. Shen, and M. Liu, "A GPS-aided omnidirectional visual-inertial state estimator in ubiquitous environments," in *Proc. IEEE/RSJ Int. Conf. Intell. Robots Syst. (IROS)*. IEEE, 2019, pp. 7750–7755.

[24] R. Mascaro, L. Teixeira, T. Hinzmann, R. Siegwart, and M. Chli, "GOMSF: Graph-optimization based multi-sensor fusion for robust UAV pose estimation," in *Proc. IEEE Int. Conf. Robot. Autom. (ICRA)*. IEEE, 2018, pp. 1421–1428.

[25] Z. Zhang, H. Wang, and W. Chen, "A real-time visual-inertial mapping and localization method by fusing unstable GPS," in *13th World Congr. Int. Control Autom. (WCICA)*. IEEE, 2018, pp. 1397–1402.

[26] T. D. Barfoot, *State estimation for robotics*. Cambridge University Press, 2017.

[27] A. Gadwe and H. Ren, "Real-time 6DoF pose estimation of endoscopic instruments using printable markers," *IEEE Sens. J.*, vol. 19, no. 6, pp. 2338–2346, 2018.

[28] Y. Zhuang, L. Hua, L. Qi, J. Yang, P. Cao, Y. Cao, Y. Wu, J. Thompson, and H. Haas, "A survey of positioning systems using visible LED lights," *IEEE Commun. Surveys Tuts.*, vol. 20, no. 3, pp. 1963–1988, 2018.

[29] J. Armstrong, Y. Sekercioglu, and A. Neild, "Visible light positioning: a roadmap for international standardization," *IEEE Commun. Mag.*, vol. 51, no. 12, pp. 68–73, 2013.

[30] N. U. Hassan, A. Naeem, M. A. Pasha, T. Jadoon, and C. Yuen, "Indoor positioning using visible LED lights: A survey," *ACM Computing Surveys (CSUR)*, vol. 48, no. 2, pp. 1–32, 2015.

[31] L. Li, P. Hu, C. Peng, G. Shen, and F. Zhao, "Epsilon: A visible light based positioning system," in *Proc. NSDI'14*, 2014, pp. 331–343.

[32] A. Jovicic, "Qualcomm Lumicast: A high accuracy indoor positioning system based on visible light communication," 2016.

[33] Y.-S. Kuo, P. Pannuto, K.-J. Hsiao, and P. Dutta, "Luxapose: Indoor positioning with mobile phones and visible light," in *Proc. MobiCom'14*. ACM, 2014, pp. 447–458.

[34] H.-Y. Lee, H.-M. Lin, Y.-L. Wei, H.-I. Wu, H.-M. Tsai, and K. C.-J. Lin, "Rollinglight: Enabling line-of-sight light-to-camera communications," in *Proc. MobiSys'15*. ACM, 2015, pp. 167–180.

[35] Y. Yang, J. Hao, and J. Luo, "CeilingTalk: Lightweight indoor broadcast through LED-camera communication," *IEEE Trans. Mobile Comput.*, vol. 16, no. 12, pp. 3308–3319, 2017.

[36] G. Simon, G. Zachár, and G. Vakulya, "Lookup: Robust and accurate indoor localization using visible light communication," *IEEE Trans. Instrum. Meas.*, vol. 66, no. 9, pp. 2337–2348, 2017.

[37] C. Qin and X. Zhan, "VLIP: Tightly coupled visible-light/inertial positioning system to cope with intermittent outage," *IEEE Photon. Technol. Lett.*, vol. 31, no. 2, pp. 129–132, 2018.

[38] Q. Liang and M. Liu, "A tightly coupled VLC-inertial localization system by EKF," *IEEE Rob. Autom. Lett.*, vol. 5, no. 2, pp. 3129–3136, 2020.

[39] A. Yassin, Y. Nasser, M. Awad, A. Al-Dubai, R. Liu, C. Yuen, R. Raulefs, and E. Aboutanios, "Recent advances in indoor localization: A survey on theoretical approaches and applications," *IEEE Commun. Surveys Tuts.*, vol. 19, no. 2, pp. 1327–1346, 2016.

[40] M. Z. Win, Y. Shen, and W. Dai, "A theoretical foundation of network localization and navigation," *Proc. IEEE*, vol. 106, no. 7, pp. 1136–1165, 2018.

[41] S. Safavi, U. A. Khan, S. Kar, and J. M. Moura, "Distributed localization: A linear theory," *Proc. IEEE*, vol. 106, no. 7, pp. 1204–1223, 2018.

[42] M. Z. Win, A. Conti, S. Mazuelas, Y. Shen, W. M. Gifford, D. Dardari, and M. Chiani, "Network localization and navigation via cooperation," *IEEE Commun. Mag.*, vol. 49, no. 5, pp. 56–62, 2011.

[43] K. Pahlavan, X. Li, and J.-P. Makela, "Indoor geolocation science and technology," *IEEE Commun. Mag.*, vol. 40, no. 2, pp. 112–118, 2002.

[44] A. Conti, S. Mazuelas, S. Bartoletti, W. C. Lindsey, and M. Z. Win, "Soft information for localization-of-things," *Proc. IEEE*, vol. 107, no. 11, pp. 2240–2264, 2019.

[45] M. F. Keskin, A. D. Sezer, and S. Gezici, "Localization via visible light systems," *Proc. IEEE*, vol. 106, no. 6, pp. 1063–1088, 2018.

[46] A. Conti, M. Guerra, D. Dardari, N. Decarli, and M. Z. Win, "Network experimentation for cooperative localization," *IEEE J. Sel. Areas Commun.*, vol. 30, no. 2, pp. 467–475, 2012.

[47] Y. Nakazawa, H. Makino, K. Nishimori, D. Wakatsuki, and H. Komagata, "Indoor positioning using a high-speed, fish-eye lens-equipped camera in visible light communication," in *Proc. Int. Conf. Indoor Positioning Indoor Navigat. (IPIN)*. IEEE, 2013, pp. 1–8.

[48] Y. Li, Z. Ghassemlooy, X. Tang, B. Lin, and Y. Zhang, "A VLC smartphone camera based indoor positioning system," *IEEE Photon. Technol. Lett.*, vol. 30, no. 13, pp. 1171–1174, 2018.

[49] M. Rátosi and G. Simon, "Real-time localization and tracking using visible light communication," in *Proc. Int. Conf. Indoor Positioning Indoor Navigat. (IPIN)*. IEEE, 2018, pp. 1–8.

[50] K. Qiu, F. Zhang, and M. Liu, "Let the light guide us: VLC-based localization," *IEEE Robot. Autom. Mag.*, vol. 23, no. 4, pp. 174–183, 2016.

[51] Q. Liang, L. Wang, Y. Li, and M. Liu, "Plugo: a scalable visible light communication system towards low-cost indoor localization," in *Proc. IEEE/RSJ Int. Conf. Intell. Robots Syst. (IROS)*. IEEE, 2018, pp. 3709–3714.

[52] C. Zhang and X. Zhang, "LiTell: robust indoor localization using unmodified light fixtures," in *Proc. 22nd Annu. Int. Conf. Mobile Comput. Netw. (MobiCom)*. ACM, 2016, pp. 230–242.

[53] ——, "Pulsar: Towards ubiquitous visible light localization," in *Proc. 23rd Annu. Int. Conf. Mobile Comput. Netw. (MobiCom)*. ACM, 2017, pp. 208–221.

[54] S. Zhu and X. Zhang, "Enabling high-precision visible light localization in today's buildings," in *Proc. 15th Int. Conf. Mobile Syst., Appl., Services (MobiSys)*. ACM, 2017, pp. 96–108.

[55] Q. Xu, R. Zheng, and S. Hranilovic, "IDyLL: Indoor localization using inertial and light sensors on smartphones," in *Proc. Int. Joint Conf. Pervasive Ubiquitous Comput. (UbiComp)*. ACM, 2015, pp. 307–318.

[56] A. R. Jiménez, F. Zampella, and F. Seco, "Improving inertial pedestrian dead-reckoning by detecting unmodified switched-on lamps in buildings," *Sensors*, vol. 14, no. 1, pp. 731–769, 2014.

[57] Y. Nakazawa, H. Makino, K. Nishimori, D. Wakatsuki, and H. Komagata, "LED-tracking and ID-estimation for indoor positioning using visible light communication," in *Proc. Int. Conf. Indoor Positioning Indoor Navigat. (IPIN)*. IEEE, 2014, pp. 87–94.

[58] Q. Liang, Y. Sun, and M. Liu, "Supplementary material to: A novel inertial-aided visible light positioning system using modulated leds and unmodulated lights as landmarks," 2020. [Online]. Available: https://ram-lab.com/papers/2020/tase20vlc-supp.pdf

[59] A. M. Andrew, "Multiple view geometry in computer vision," *Kybernetes*, 2001.

[60] J. Munkres, "Algorithms for the assignment and transportation problems," *J. Soc. Ind. Appl. Math.*, vol. 5, no. 1, pp. 32–38, 1957.

[61] M. Liu, K. Qiu, F. Che, S. Li, B. Hussain, L. Wu, and C. P. Yue, "Towards indoor localization using visible light communication for consumer electronic devices," in *Proc. IEEE/RSJ Int. Conf. Intell. Robots Syst. (IROS)*. IEEE, 2014, pp. 143–148.

[62] N. Trawny and S. I. Roumeliotis, "Indirect Kalman filter for 3D attitude estimation," *University of Minnesota, Dept. of Comp. Sci. & Eng., Tech. Rep*, vol. 2, p. 2005, 2005.

[63] M. Li, H. Yu, X. Zheng, and A. I. Mourikis, "High-fidelity sensor modeling and self-calibration in vision-aided inertial navigation," in *Proc. IEEE Int. Conf. Robot. Autom. (ICRA)*. IEEE, 2014, pp. 409–416.

[64] P. Furgale, J. Rehder, and R. Siegwart, "Unified temporal and spatial calibration for multi-sensor systems," in *Proc. IEEE/RSJ Int. Conf. Intell. Robots Syst. (IROS)*. IEEE, 2013, pp. 1280–1286.

[65] J. Sturm, N. Engelhard, F. Endres, W. Burgard, and D. Cremers, "A benchmark for the evaluation of RGB-D SLAM systems," in *Proc. IEEE/RSJ Int. Conf. Intell. Robots Syst. (IROS)*. IEEE, 2012, pp. 573–580.

[66] Q. Liang and M. Liu, "An automatic site survey approach for indoor localization using a smartphone," *IEEE Trans. Autom. Sci. Eng.*, vol. 17, no. 1, pp. 191–206, 2019.

[67] R. Liu, S. H. Marakkalage, M. Padmal, T. Shaganan, C. Yuen, Y. L. Guan, and U.-X. Tan, "Collaborative SLAM based on Wifi fingerprint similarity and motion information," *IEEE Internet Things J.*, vol. 7, no. 3, pp. 1826–1840, 2019.

[68] Z. Zhang and D. Scaramuzza, "A tutorial on quantitative trajectory evaluation for visual (-inertial) odometry," in *Proc. IEEE/RSJ Int. Conf. Intell. Robots Syst. (IROS)*. IEEE, 2018, pp. 7244–7251.

[69] A. Geiger, P. Lenz, and R. Urtasun, "Are we ready for autonomous driving? the KITTI vision benchmark suite," in *Proc. IEEE Int. Conf. Comput. Vis. Pattern Recog. (CVPR)*. IEEE, 2012, pp. 3354–3361.

[70] N. Otsu, "A threshold selection method from gray-level histograms," *IEEE Trans. Syst., Man, Cybern.*, vol. 9, no. 1, pp. 62–66, 1979.

Qing Liang (Member, IEEE) received his B.A. degree in Automation from Xi'an Jiaotong University, Xi'an, China, in 2013 and his master's degree in instrument science and technology from Beihang University, Beijing, China, in 2016. He is currently pursuing his Ph.D. degree with the Department of Electronic and Computer Engineering, The Hong Kong University of Science and Technology, Hong Kong. His current research interests include sensor fusion, low-cost localization, and mobile robots.

Yuxiang Sun (Member, IEEE) received the Ph.D. degree from The Chinese University of Hong Kong, Shatin, Hong Kong, in 2017, the master's degree from the University of Science and Technology of China, Hefei, China, in 2012, and the bachelor's degree from the Hefei University of Technology, Hefei, China, in 2009. He is now a research assistant professor at the Department of Mechanical Engineering, The Hong Kong Polytechnic University, Hung Hom, Hong Kong. Prior to that, he was a research associate at the Department of Electronic and Computer Engineering, The Hong Kong University of Science and Technology, Clear Water Bay, Hong Kong. He serves as an Associate Editor of IEEE Robotics and Automation Letters. Dr. Sun's research interests include autonomous driving, artificial intelligence, deep learning, mobile robots, etc.

Lujia Wang (Member, IEEE) received the Ph.D. degree from the Department of Electronic Engineering, The Chinese University of Hong Kong, Shatin, Hong Kong, in 2015. She is now a research assistant professor at the Department of Electronic and Computer Engineering, The Hong Kong University of Science and Technology, Hong Kong. From 2016 to 2021, she was an associate professor with the Shenzhen Institutes of Advanced Technology, Chinese Academy of Sciences, Shenzhen, Guangdong. From 2015 to 2016, she was a research fellow with the School of Electrical Electronic Engineering, Nanyang Technological University, Singapore. Her current research interests include Cloud Robotics, Lifelong Federated Robotic Learning, Resource/Task Allocation for Robotic Systems, and Applications on Autonomous Driving, etc.

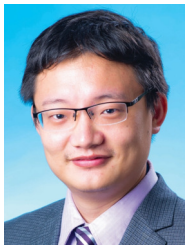

Ming Liu (Senior Member, IEEE) received his B.A. degree in Automation from Tongji University, Shanghai, China, in 2005 and his Ph.D. degree from the Department of Mechanical and Process Engineering, ETH Zürich, Zürich, Switzerland, in 2013.

During his master's study at Tongji University, he stayed one year in Erlangen-Nünberg University and Fraunhofer Institute IISB, Germany, as a master visiting scholar. He is currently with the Department of Electronic and Computer Engineering, the Department of Computer Science and Engineering, and the Robotics Institute, The Hong Kong University of Science and Technology, Hong Kong. His research interests include dynamic environment modeling, deep-learning for robotics, 3-D mapping, machine learning, and visual control.

Prof. Liu was a recipient of the Best Student Paper Award at the IEEE International Conference on Multisensor Fusion and Integration for Intelligent Systems 2012, the Best Paper in Information Award at the IEEE International Conference on Information and Automation 2013, the Best RoboCup Paper at the IEEE/RSJ International Conference on Intelligent Robots and Systems 2013, and twice the Winning Prize of the Chunhui-Cup Innovation Contest.